Multiple origins of hornblende-rich cumulates within a deep magma reservoir from the Late Jurassic Gangdese arc, south Tibet: implications for arc crustal evolution

Tong−Yu Huang[a], Qiang Wang[a,b*], Andrew C. Kerr[c], Jun Wang[a], Zi−Qi Jiang[d], Lin Ma[a]

[a] *State Key Laboratory of Deep Earth Processes and Resources, Guangzhou Institute of Geochemistry, Chinese Academy of Sciences, Guangzhou 510640, PR China*

[b] *College of Earth and Planetary Sciences, University of Chinese Academy of Sciences, Beijing 100049, China*

[c] *School of Earth and Environmental Sciences, Cardiff University, Cardiff, CF10 3AT, UK*

[d] *School of Earth Science and Guangxi Key Laboratory of Hidden Metallic Ore Deposits Exploration, Guilin University of Technology, Guilin, 541004*

[*] *Corresponding authors.*

E−mail address: Qiang Wang (wqiang@gig.ac.cn)

Abstract

Early fractionation of amphibole is an essential process in the evolution of hydrous sub-arc mantle-derived magmas. However, the petrogenesis of hornblende-rich cumulates in the deep crust and their significant role in arc crustal evolution remains unclear. In this contribution, we focus on Late Jurassic mafic-ultramafic intrusive rocks from the Zedong terrane (central-eastern Gangdese area, South Tibet) and use detailed petrographic, mineralogical and geochemical data to determine the origin of hornblende-rich cumulates with textural and chemical heterogeneities. The clinopyroxene (Cpx) hornblendite with adcumulate texture contains three distinct types of amphibole (cumulus, poikilitic, and minor interstitial). These amphiboles display homogeneous major and trace element compositions, consistent with crystallization from a liquid of constant composition. Rock fabric analysis further suggests that they formed by in-situ nucleation and overgrowth at the interface between the mush layer and the convecting parental magma within the magma reservoir. Type I hornblende (Hb) gabbros have an orthocumulate texture with the lowest whole-rock MgO and Mg# values. Intercumulus melt evolution revealed by mineral assemblage and compositional variations indicate that Type I gabbros formed through a peritectic reaction between clinopyroxene precursors and evolved interstitial melts, followed by melt migration and fluid exsolution in a semi-open system. Type II gabbros have the highest whole-rock MgO and Mg# values and are characterized by extensive disequilibrium features. Geochemical modeling indicates that their formation entails a melt-flushing process involving the upward percolation of deep-recharge melts through the crystal mush. This

study provides petrological evidence for the multiple origins of hornblende-rich cumulates within a common middle−lower crustal magma reservoir. Their textural and chemical heterogeneities may reflect spatial variations in crystallization regimes across distinct reservoir domains. The Zedong hornblende-rich cumulates have more depleted whole-rock Sr–Nd isotopic compositions and zircon $\varepsilon_{Hf}(t)$ values than those cumulates from Early Jurassic and Cretaceous Gangdess arc. This indicates that their parental magma was derived from a more juvenile mantle wedge and records significant growth in the middle−lower crust. The Cpx hornblendite has lowest concentrations of SiO_2 but highest $Fe_2O_3^T$ and $(Dy/Yb)_N$ ratios. The differentiation trends between the cumulate rocks and coeval non-cumulate rocks within the Zedong terrane indicate that the evolution of the Late Jurassic arc crust was mainly controlled by amphibole fractionation. Modeling shows that melts in equilibrium with the cumulus and brown amphiboles are compositionally analogous to coeval intermediate-acid rocks, and imply the existence of a trans-crustal magma plumbing system in this arc.

1. INTRODUCTION

Unravelling the evolution and differentiation of hydrous primary, mantle-derived arc magmas is important in understanding the formation of continental crust (Ducea et al., 2015). Geochemical characteristics of arc lava suites have demonstrated that the fractionation of amphibole within the deep arc crust is widespread during the evolution of arc magmas (Davidson et al., 2007). Furthermore, amphibole-rich cumulates are a common component of the ancient magmatic arc lower crust such as the Bonanza arc,

Canada (Larocque & Canil, 2010); the Talkeetna arc, south-central Alaska (Greene et al., 2006); the Kohistan arc, Pakistan (Burg et al., 2005); Fiordland, New Zealand (Daczko et al., 2016); the North Cascades, USA (Dessimoz et al., 2012); the Famatinian arc, Argentina (Walker et al., 2015); and the Gangdese Batholith, southern Tibet (Xu et al., 2019; Guo et al., 2020). Extensive research on the Kohistan arc system has demonstrated that hydrous (or super-hydrous) liquid lines of descent generate lower crustal rocks with amphibole as the dominant fractionating phase (Jagoutz et al., 2011; Jagoutz & Kelemen, 2015; Urann et al., 2022). Significantly, fractional crystallization experiments closely reproduce the compositions of natural rocks, notably replicating the cumulate sequences observed in the roots of the Kohistan arc (Alonso-Perez & Müntener, 2009; Müntener & Ulmer, 2018). Compared to mature magmatic arcs, as exemplified by the Sierra Nevada in the North Cordillera, which show a crystallization sequence from high-Mg pyroxenite to low-Mg plagioclase-rich pyroxenite (Lee et al., 2006). Fractionation of amphibole, with significantly lower SiO_2 and a high FeO/MgO ratio than primary basalt, increases residual melt SiO_2 and drives calc-alkaline trends more efficiently than that of gabbroic assemblages, which exert limited leverage on silica enrichment (Davidson et al., 2007; Krawczynski et al., 2012). The delamination of dense amphibole-rich cumulates provides a key mechanism for generating the andesitic composition of the continental crust (Jagoutz et al., 2011; Müntener & Ulmer, 2018). Conversely, the preservation and subsequent remelting of these cumulates is an equally important process. Experimental studies and thermodynamic modeling confirm that amphibole-rich lithologies can act as fertile sources for partial melting under lower

crustal conditions, significantly enhancing melt productivity and producing felsic melts (Peacock et al., 1994; Sen & Dunn, 1994; Rapp & Watson, 1995; Sisson et al., 2005). Therefore, the remelting of amphibole-rich (ultra) mafic cumulates contributes to intra-crustal differentiation, thereby enhancing the chemical maturation and stratification of juvenile arc crust (Zhu et al., 2022, 2023).

The formation of cumulates necessitates the separation of crystals from the remaining liquid, the conventional model centers on gravitationally driven compaction and the consequent liquid expulsion (Wager et al., 1960). Based on the relative proportions of "trapped liquid" defined as the liquid component trapped between the cumulus crystals once the mixture has become geochemically isolated from the parent magma (Latypov et al., 2023), cumulates are sub-divided into adcumulates (<5 vol.%) and orthocumulates (>20 vol.%) (Holness, 2021). The solidification of a cumulate begins with the assembly of primocrysts to form a crystal mush, either by re-distribution from elsewhere in the intrusion (Wager & Brown, 1968; Higgins, 1991; Namur et al., 2011; Barnes et al., 2021) or by in situ nucleation and growth (Campbell, 1978; McBirney & Noyes, 1979; Holness, 2021; Latypov et al., 2023). Orthocumulates form in a closed system after initial crystal accumulation, while adcumulates require increasingly open-system conditions throughout solidification (Holness, 2021). However, amphibole-rich cumulates often develop at the expense of clinopyroxene (±olivine) through a reaction-replacement mechanism. This process, which has been widely reported from exhumed crustal sections and xenoliths throughout the world (Best, 1975; Conrad & Kay, 1984; DeBari et al., 1987; Costa et al., 2002; Larocque &

Canil, 2010; Tiepolo et al., 2011, 2012; Smith, 2014; Cooper et al., 2016; Blatter et al., 2017; Perinelli et al., 2017; Xu et al., 2019, 2021; Wang et al., 2019; Chang et al., 2021) and from melting or crystallization experimental products of basalts (Yoder & Tilley, 1962; Holloway & Burnham, 1972; Cawthorn et al., 1973; Helz, 1973; Foden & Green, 1992; Ulmer et al., 2018). Typically, the microtextural evidence for peritectic replacement is preserved as vestiges of resorbed clinopyroxene chadacrysts within amphibole. In some cases, clinopyroxene relicts are completely overprinted by amphibole with a granoblastic texture (Smith, 2014; Zhu et al., 2024) involves channelized reactive melt flow through porous mush (Nixon et al., 2024). In contrast, idiomorphic framework amphibole adcumulates formed by direct precipitation from a melt are relatively uncommon (e.g. Santana et al., 2020; Sosa et al., 2023). Although the two genetic types of amphibole (primary cumulate phase vs. reaction-replacement origin) can be distinguished (Smith, 2014; Zhu et al., 2024), the primary factors controlling their formation remain unclear, particularly when both rock types occur within the same magmatic system.

The Gangdese arc (southern Tibet) recorded the initial growth of continental arc crust during Mesozoic Neo-Tethys oceanic subduction (Zhu et al., 2023). The fractional crystallization of pre-collisional arc magmas resulted in the formation of abundant hornblende-rich cumulates (e.g., hornblendite and hornblende gabbro) in the Gangdese lower crust (Zhu et al., 2022) and this makes them ideal candidates for investigating the role of amphibole in arc crustal evolution. These hornblende-rich cumulates are found at Cuijiu (Xu et al., 2019, 2021) and Milin (Ma et al., 2013; Guo et al., 2020) and formed

in the Late Triassic and Late Cretaceous respectively (Fig. 1b). Recent research has identified Late Jurassic hornblende-rich mafic-ultramafic intrusive rocks in the Zedong terrane within the central-eastern Gangdese arc. Here we present the results of an integrated study involving zircon U-Pb geochronology, whole-rock geochemistry and mineral geochemistry of these intrusive rocks. These new data are combined with detailed field relationships, petrographic and mineralogical observations to determine the multiple origins of hornblende-rich cumulates with textural and chemical heterogeneities within a common middle-lower crustal magma reservoir. The influence of amphibole differentiation on arc crustal evolution is also elucidated by assessing the relationship between cumulate and coeval non-cumulate rocks.

2. GEOLOGICAL BACKGROUND

The Tibetan Plateau consists of the Kunlun-Qaidam, Songpan-Ganze, Qiangtang, Lhasa and Himalaya Blocks (Fig. 1a). The Lhasa Block in southern Tibet has long been accepted as the last geological block accreted to Eurasia before its collision with the northward drifting Indian subcontinent in the early Cenozoic (Zhu et al., 2011). Based on the distribution of different sedimentary cover rocks and ophiolites, the Lhasa Block has recently been divided into northern, central, and southern sub-blocks, separated by the Shiquan River-Nam Tso Mélange zone (SNMZ) and Luobadui-Milashan fault (LMF), respectively (Pan et al., 2006; Zhu et al., 2011). The southern Lhasa sub-block was an active continental margin (the Gangdese arc) accompanying northward Neo-Tethyan subduction (Searle et al., 1987). The arc magmatic activity in the Gangdese arc

158 lasted from the middle Triassic to the middle Miocene (c. 240−10 Ma) and consists
159 mainly of the voluminous Gangdese Batholith and coeval terrestrial volcanic
160 successions that include the Lower-Middle Jurassic, the Cretaceous and the Paleocene-
161 Eocene Linzizong Group (Zhu et al., 2018).

162 The Indus-Yarlung Zangbo suture zone (IYZSZ) consists of several geological
163 units, and from north to south, there are the Gangdese magmatic belt, the Xigaze forearc
164 basin, the Yarlung-Zangbo ophiolite belt and Tethyan Himalayan sedimentary strata
165 (Fig. 1b). The Zedong terrane, first described by Aitchison et al. (2000), is found in the
166 eastern part of the IYZSZ and extends about 15 km from east to west and outcrops an
167 area of about 25 km^2 near Zedong town. The Zedong terrane is sandwiched between
168 the Gangdese batholith to the north and the Yarlung-Zangbo Ophiolite Mélange to the
169 south, and they are separated by the Renbu-Zedong thrust (RZT) (Fig. 1c). The Zedong
170 terrane was formed during the Late Jurassic. McDermid et al. (2002) reported zircon
171 U-Pb ages of 157−163 Ma for both volcanic (dacite breccia and dykes) and plutonic
172 rocks (quartz diorites), which are slightly older than Ar-Ar ages of hornblendes (i.e.,
173 ~152−158 Ma). More recently, Wang et al. (2012) reported a U-Pb age of 157.5±1.4
174 Ma for zircons from a granodiorite sample and samples of different lithologies,
175 including hornblendites, gabbros, andesites and tonalites, systematically yielded zircon
176 U-Pb ages of 155−160 Ma (Zhang et al., 2014).

177 The tectonic character of Zedong terrane has been a subject of controversy.
178 Previous studies have proposed that it represents the remnants of an intra-oceanic arc
179 developed within the Neo-Tethys Ocean since the Late Jurassic (Aitchison et al., 2000;

McDermid et al., 2002; Wang et al., 2012). Alternatively, Zhang et al., (2014) suggests that the Zedong terrane represents a slice of the active continental margin developed on the southern margin of the Lhasa Block, given that magmatic rocks in the Zedong terrane show compositional similarities with the Jurassic rocks exposed in the Gangdese arc. The current tectonic location may be related to subduction erosion during the Early Cretaceous, which caused the truncation of forearc crust and extremely short arc-suture distance (Hunag et al., 2022).

3. FIELD OBSERVATIONS AND PETROGRAPHY

The Zedong terrane mainly incorporates volcanic and volcaniclastic rocks including basaltic-andesitic pillow lavas, breccias, tuffs, flows, cherty tuffs, dacites and rhyolites. In addition, plutons including mafic-ultramafic cumulate rocks, diorites, quartz diorites and granitic rocks are sporadically exposed (McDermid et al., 2002; Zhang et al., 2014). The mafic-ultramafic intrusive rocks in this study consist of hornblendites and gabbros. The gabbros are exposed to the east and west of Zedong town, while the hornblendites outcrop only on the east side (Fig. 1c). The structural relationship between the hornblendites and gabbros can be observed on the outcrop of the section near the Zecuoba Temple, east of Zedong town. The hornblendites are exposed in association with some of the gabbros, and the boundary between hornblendites and gabbros is very irregular (Fig. 2a) while other gabbro outcrops contain dark hornblendite inclusions (20-30 cm; Fig. 2b). The hornblendite and gabbro commonly have a dark green color with massive textures, and all of the rocks are

202 petrographically unweathered in hand specimen (Fig. 2). Representative samples
203 belonging to different rock types have been collected for detailed study. Table 1 shows
204 a summary of the general petrographic features of the samples.
205
206 ***Clinopyroxene hornblendite***
207 The hornblendites display adcumulate textures with dominant euhedral
208 clinopyroxene and euhedral to subhedral amphibole (combined ＞90 vol. %) (Fig. 3a
209 −c). Sample 09TB01−2 consists mainly of medium- to coarse-grained brown amphibole
210 (~60 vol. %, most <1 mm), medium- to fine-grained clinopyroxene (~30 vol. %), and
211 magnetite (~10 vol. %) (Fig. 3a). Sample 09TB01−1 consists mainly of medium- to
212 coarse-grained brown amphibole (~65 vol. %, most >2 mm), medium-grained
213 clinopyroxene (~25 vol. %, 0.5−2 mm), subordinate magnetite (~10 vol. %) and trace
214 anhedral apatite occurs within the amphibole and clinopyroxene grains or in the
215 interstices between them. The distribution of amphibole in the hornblendites occurs in
216 three distinct microtextural settings: (1) dominant cumulus phase (Fig. 3a, b); (2) large
217 amphibole oikocrysts enclosing rounded magnetite and clinopyroxene (Fig. 3b, c); (3)
218 minor interstitial anhedral grains (Fig. 3c) (＜5 vol. %). The amphibole contains some
219 rounded clinopyroxene inclusions and a few inclusions are altered to epidote (Fig. 3a).
220 The hornblendites contain more than 10 vol. % clinopyroxene and so we refer to these
221 rocks as “clinopyroxene (Cpx) hornblendites”.
222
223 ***Hornblende gabbro***

The gabbros have been divided into two groups based on mineral assemblage, proportion and grain size. Group I are characterized by orthocumulate textures, and consist mainly of brown amphibole (~>70 vol. %) and interstitial euhedral to subhedral green amphibole (<10 vol. %), as well as interstitial plagioclase (~15 vol. %), quartz (~5 vol. %) and trace magnetite (Fig. 3d). The brown amphibole can be subdivided into three types based on morphology: (1) amphibole with a dominant granoblastic texture (>50 vol. %; Fig. 3d); (2) idiomorphic amphibole (<10 vol. %; Fig. 3e); and (3) minor amphibole containing resorbed clinopyroxene chadacrysts (<5 vol. %; Fig. 3f). However, relict clinopyroxene inclusions and some amphiboles are altered to chlorite, and interstitial plagioclase commonly replaced by epidote and sericite.

Group II gabbros are generally orthocumulates, and are dominated by subhedral to anhedral amphibole (60–65 vol. %), rounded and embayed clinopyroxene inclusions (10–15 vol. %) and interstitial plagioclase (15–20 vol. %) which are mostly altered to clay (Fig. 4a). The amphibole oikocrysts contain abundant anhedral dispersed grains of relict clinopyroxene inclusions (0.5−1 mm) (Fig. 4a). Amphibole blebs are found along the cleavage planes of some clinopyroxene inclusions (Fig. 4a). Some amphiboles are characterized by brown cores and green rims (Fig. 4c). In addition, some clinopyroxene grains have disequilibrium dissolution features such as embayed edges and resorption channels (Fig. 4a−c). These textural relationships are indicative of a clinopyroxene-consuming peritectic reaction (Smith, 2014; Wang et al., 2019; Xu et al., 2021). Apatite can coexist with clinopyroxene and can occur both as early-crystallized inclusions within large amphibole oikocrysts, and as a late interstitial phase between the

intercumulus amphibole (Fig. 4a-b), indicating a wide range of crystallization temperatures. In addition, some of the clinopyroxene inclusions are mostly altered to chlorite and epidote, matrix minerals (5−10 vol. %) are mostly altered to epidote and sericite. With plagioclase contents exceeding 10 vol. % and mafic mineral assemblages dominated by amphibole rather than clinopyroxene, these two groups of gabbro meet the criteria for "hornblende (Hb) gabbro" in the classification of mafic intrusive rocks (McBirney, 2007).

4. ANALYTICAL METHODS

Zircons were separated from sample 09TB143 using conventional heavy liquid and magnetic separation techniques (Li & Tan, 1998), and then were mounted in epoxy and polished. The zircons were imaged prior to U-Pb analysis using cathodoluminescence (CL) imaging employing a JEOL JXA-8100 Superprobe at the State Key Laboratory of Isotope Geochemistry, Guangzhou Institute of Geochemistry, Chinese Academy of Sciences, Guangzhou, China (SKLaBIG, GIG, CAS), in order to characterize internal structures and choose potential target sites for U-Pb dating and Hf isotopic analyses.

Zircon laser ablation inductively coupled plasma mass spectrometry (LA-ICP-MS) U-Pb analyses were carried out at the Institute of Geology and Geophysics, Chinese Academy of Sciences (IGGCAS), Beijing, China. Laser ablation was conducted using an Agilent 7500a Q-ICP-MS equipped with a 193−nm Excimer ArF laser ablation system (Geolas plus), using zircon 91500 as external standard with circle spot of 30 μm

in diameter. The detailed analytical procedures for zircon U-Pb age can be found in Xie et al. (2008). $^{207}Pb/^{235}U$ and $^{206}Pb/^{238}U$ ratios were calculated using ICPMSDataCal software (Liu et al., 2009). Common Pb was corrected according to the method outlined by Andersen (2002) and weighted-mean U-Pb ages and concordia plots were generated using Isoplot/Ex v.3.0 (Ludwig, 2003). Analyses of the zircon standard GJ-1 as an unknown yielded a weighted mean $^{206}Pb/^{238}U$ age of 608±6 Ma (2σ, n=4), which is in good agreement with the recommended value (Jackson et al., 2004).

In situ zircon Lu-Hf isotopic analyses were carried out on a Neptune Plus multi-collector ICP-MS equipped with a RESOlution M-50193 nm laser-ablation system (Resonetics) at the SKLaBIG, GIG, CAS. Lu-Hf isotopic analyses were conducted on the same zircon grains that were previously analyzed for U-Pb geochronology, with ablation pits of 45 μm in diameter, ablation time of 30 s, repetition rate of 6 Hz, and laser beam energy density of 4 J/cm^2. The detailed analytical procedures are similar to those described by Zhang et al. (2015). Measured $^{176}Hf/^{177}Hf$ ratios were normalized to $^{179}Hf/^{177}Hf$=0.7325 (Zhang et al., 2015). Analyses of the Plešovice zircon standard yielded a weighted mean of $^{176}Hf/^{177}Hf = 0.282476 \pm 0.000010$ (2SD; n = 6), consistent with the certified value of 0.282482 ± 0.000013 (2SD; Sláma et al., 2008).

Rock samples used for whole-rock elemental and isotopic analysis during this study were sawn into small chips, ultrasonically cleaned in distilled water with <3% HNO_3, then in MilliQ water alone, and subsequently dried and handpicked to remove visible contamination. The rocks were crushed by a jaw crusher and then powdered to ~200 mesh in an agate mortar and pestle. Major element concentrations were

290 determined on fused glass beads using a Rigaku RIX 2000 X-ray fluorescence
291 spectrometer at SKLaBIG, GIG, CAS. Calibration lines used for quantification were
292 produced by bivariate regression of data from 36 reference materials encompassing a
293 wide range of silicate compositions (Li et al., 2005), and the resulting analytical
294 uncertainties are generally ＜2%. Trace elements, including the rare earth elements
295 (REE), were determined by ICP-MS employing a Perkin-Elmer ELAN 6000 instrument
296 at SKLaBIG, GIG, CAS, and using the procedures outlined in Li et al. (2006). About
297 40 mg of each powdered sample was dissolved in a high-pressure Teflon bomb for 2
298 days at 190 ℃ using HF+HNO_3+$HClO_4$ (1:1:0.2) mixtures. The resulting analytical
299 precision for the majority of elements is ＜3%.

300 Sr and Nd isotopic analyses were undertaken on a Neptune MC-ICP-MS
301 instrument at SKLaBIG, GIG, CAS. Analytical procedures are similar to those
302 described in Li et al. (2004). Sr and REE were separated using cation columns, and Nd
303 fractions were further separated by HDEHP-coated Kef columns. The $^{87}Sr/^{86}Sr$ ratio of
304 the NBS987 standard and $^{143}Nd/^{144}Nd$ ratio of the Shin Etsu JNdi-1 standard were
305 0.710264±0.000020 (n=6, 2SD) and 0.512102±0.000012 (n=6, 2SD), respectively. All
306 measured Sr-Nd isotopic ratios were normalized to $^{146}Nd/^{144}Nd$=0.7219 and
307 $^{86}Sr/^{88}Sr$=0.1194, respectively. The Sr-Nd isotopes of USGS reference material BHVO-
308 2 of this study gave $^{87}Sr/^{86}Sr$=0.703482±0.000008 (SE),
309 $^{143}Nd/^{144}Nd$=0.512983±0.000010 (SE) (Weis et al., 2005), respectively, within the
310 analytical error of the recommended values.

311 The major element compositions of all silicate mineral analyses were carried out

312 at the SKLaBIG, GIG, CAS, using a JXA-8100 electron microprobe. An accelerating
313 voltage of 15 kV, a specimen current of 20 nA, and a beam size of 1−2 μm were
314 employed. The analytical errors are generally less than 2%. The analytical procedures
315 were described in detail in Huang et al. (2007). In situ mineral trace element
316 compositions were measured with an ELEMENT XR (Thermo Fisher Scientific) ICP-
317 SF-MS coupled with a 193−nm (ArF) Resonetics RESOlution M−50 laser ablation
318 system at SKLaBIG, GIG, CAS. All LA-ICP-MS spots were located over EMPA spots.
319 Laser condition was set as following: beam size, 45 μm; repetition rate, 6 Hz; energy
320 density, ~4 J/cm^2. A smoothing device (The Squid, Laurin Technic) was used to smooth
321 the sample signal. Each spot analysis consisted of 20 s gas blank collection with the
322 laser off, and 30 s sample signal detection with the laser on. Si was selected as the
323 internal standard element. NIST610 was selected as the calibration standard. The oxide
324 molecular yield, indicated by the $^{232}Th^{16}O/^{232}Th$ ratio, was less than 0.3%. The detailed
325 experiment procedure and data reduction strategy are described in Zhang et al. (2019).
326 NIST612 was measured as unknown samples, which indicated that most elements are
327 within 8% of the reference values and the analytical precision (2RSD) was better than
328 10% for most elements. SiO_2 contents determined by electron microprobe were used as
329 an internal standardization to normalize trace-element abundances. High-resolution
330 elemental mapping of single minerals was carried out using a JEOLJXA-8230 electron
331 probe micro-analyzer (EPMA) at the CAS Key Laboratory of Mineralogy and
332 Metallogeny. The following conditions were adopted for all grains: an accelerating
333 voltage of 20 kV, a probe current of 80 to 100 nA and a beam diameter of 5 μm. The

dwell time was set to be 40 to 60 ms for each pixel. Mg Kα and Al Kα X-rays were analyzed using a TAP crystal. Ti Kα X-rays were analyzed using a PETJ crystal and Fe Kα X-ray was analyzed using a LIFH crystal. The rock samples were observed in the backscattered electron (BSE) image mode of a Desktop SEM (Phenom XL G2) operating at an acceleration voltage of 15 kV at GIG–CAS.

Electron Backscatter Diffraction (EBSD) measurements were carried out in the Electron Microscope Center of Key Laboratory of Mineralogy and Mineralogical Sciences, CAS using a FEI Helios 5CX SEM with an Oxford Aztec Symmetry Ⅱ EBSD acquisition camera. The measurements were collected using an accelerating voltage of 20 kV, 9-μm step size, 11 μA beam current, and a working distance of 7–15 mm. The sample surface was tilted 70° relative to horizontal to enlarge beam-specimen activation surface so that EBSD signal can be enhanced. Diffraction patterns were manually collected and automatically indexed in real-time using the AZtec software from the HKL Technology, Oxford Instruments. Five to eight Kikuchi bands were included for the fitting algorithm. Only measurements with mean angular deviation (MAD) values below 1.2° were accepted for analyses, and the indexing rate is about 80%. Resulting EBSD data were then processed in AztecCrystal software.

5. ANALYTICAL RESULTS

5.1 Zircon U-Pb Ages and Hf Isotope Analyses

The data from U-Pb zircon LA-ICP-MS dating of one Hb gabbro sample (09TB143) is given in Supplementary Table S1. The majority of zircons are platy or

granular with variable grain sizes (100−150 μm) and length/width ratios vary from 1 to 1.5. The cathodoluminescence (CL) images of the zircons show no or broad-banded zoning in the core, and oscillatory zoning in the rim (Fig. S1), comparable to those reported for zircons from oceanic gabbro (Grimes et al., 2009). The analyzed zircons have Th and U contents of 292−1316 μg/g and 509−1416 μg/g, respectively, with Th/U ratios ranging from 0.5 to 1.1, consistent with those of magmatic zircons (Hoskin & Schaltegger, 2003). Moreover, no inherited cores and no significantly older zircon were found in any of the analyzed zircons. This indicates that the analyzed zircons are phenocrysts rather than xenocrysts. Fifteen spots yield Late Jurassic $^{206}Pb/^{238}U$ ages from 157 to 159 Ma and give a weight mean age 158.3±0.6 Ma (n=15; MSWD=0.31) (Fig. S1), identical to other dated samples in literature (Zhang et al., 2014).

We also carried out zircon in situ Hf isotopic analysis (with a spot size of 40 μm) for sample 09TB143, mostly on the dated spots, or adjacent to the dated spots, that had similar CL characteristics. All the dated zircons show initial $^{176}Hf/^{177}Hf$ ratios ranging from 0.283026 to 0.283139 (mean = 0.283072 ± 0.000070, 2SD), corresponding to $\varepsilon_{Hf}(t)$ values range from +12.5 to +16.4 (mean = +14.1 ± 2.5, 2SD). The analytical results are given in Supplementary Table S2.

5.2 Whole-Rock Geochemistry

Whole-rock geochemical data are presented in Table 2. The loss-on-ignition (LOI) values of Zedong mafic-ultramafic intrusive rocks vary from 1.8 wt. % to 3.8 wt. %. The Cpx hornblendite and the Hb gabbro vary greatly in terms of whole-rock

composition. The Cpx hornblendite has the lowest concentrations of SiO_2 (38.7−39.9 wt. %) but the highest concentrations of TiO_2 (1.3−1.6 wt. %), CaO (16.4−16.5 wt. %) and $Fe_2O_3^T$ (15.2−16.8 wt. %) among these rocks (Fig. 5 and Fig. S2). The two groups of gabbro have significantly different major element compositions, with Group I having lower MgO contents (4.0−6.8 wt. %) and Mg# values [47−54; where Mg# = molar 100 × Mg/(Mg + Fe_{total})] than Group II (MgO=10.7−13.1 wt. %; Mg#=67−71), but the former having more variable SiO_2 contents (43.5−51.4 wt. %) than the latter (45.4−46.5 wt. %) (Fig. 5c−d).

The Cpx hornblendite is characterized by high middle REE (MREE) concentrations and MREE to heavy REE (HREE) ratios (e.g., $(Dy/Yb)_N$=1.79−1.80) but low $(La/Yb)_N$ (2.04−2.68) ratios (subscript N denotes normalized to the chondrite values of Sun & McDonough (1989)) with no Eu anomalies (δEu=0.98−1.01; $\delta Eu=2*Eu_N/(Sm_N+Gd_N)$) (Fig. 6a). Both two groups of gabbro show subparallel REE patterns with slightly enriched ($(La/Yb)_N$=1.85−5.16) LREEs and relatively flat to depleted MREEs and HREEs ($(Dy/Yb)_{N=}$1.07−1.36), but Group I have slightly positive Eu anomalies (δEu=1.07−1.19) whereas Group II show virtually no anomaly (δEu=1.02−1.05) (Fig. 6c). As shown in the primitive mantle normalized trace-element diagram (Fig. 6b), the Cpx hornblendites are slightly enriched in large ion lithophile elements (LILE, e.g., Rb, Ba) and Pb with Zr depletion and no Nb-Ta depletion. Group I gabbros are enriched in LILE (e.g., Rb, Ba and Sr) but depleted in high field strength element (HFSE; e.g., Nb, Ta, Zr and Ti), and the Group II gabbros have variable Rb, Ba, Th, U and Pb contents (Fig. 6d).

Whole-rock initial Sr-Nd isotopic ratios of Zedong mafic-ultramafic intrusive rocks were calculated at 158 Ma. The Cpx hornblendite and the Hb gabbro have variable initial $(^{87}Sr/^{86}Sr)_i$ ratios (0.7040–0.7046), but relatively uniform εNd(t) values (+5.4 to +6.2). The variable Sr but relatively uniform Nd isotopic compositions of Hb gabbro are most likely related to significant amounts of alteration (Fig. S2g), such as the pervasive saussuritization of the majority of the plagioclase (Fig. 3-4). This inference is further corroborated by a positive correlation between $^{87}Sr/^{86}Sr$ and LOI (loss on ignition) values (Fig. S2h).

5.3 Mineral Compositions

Major oxide data and trace element data for hornblende, clinopyroxene and plagioclase are given in Supplementary Table 3−7.

Amphibole

Amphibole formulae have been calculated using the spreadsheet of Locock (2014). The amphibole cation concentrations, calculated as atoms per formula unit (apfu), are provided in Supplementary Table 3. Most of the amphiboles analyzed during this study are calcic (Fig. 7a−b; $Ca_B \geqslant 1.5$; Ti $<$ 0.5 apfu) using the nomenclature of Leake et al. (1997). Amphibole in the hornblendites show the distinct textural regions described above, however, core to rim profiles of amphibole grains indicate that zoning appears to be limited with no systematic compositional differences detected between the cumulus and interstitial crystals. The amphibole within the Cpx hornblendite are all

magnesio-hastingsite [^{A}(Na + K + 2Ca) > 0.5 apfu; ^{VI}Al ≤ Fe^{3+}] (Fig. 7a). They have almost identical major and trace element compositions, including similar REE patterns. They are characterized by the lowest SiO_2 (40.1−42.4 wt. %) and MgO (13.3−14.0 wt. %), but the highest Al_2O_3 (12.8−14.3 wt. %) and TiO_2 (1.8−2.5 wt. %) contents relative to those in the two groups of Hb gabbros (Fig. 8). The chondrite-normalized REE patterns are bell-shaped with LREE- and HREE-depleted relative to MREE without obvious Eu anomalies (Fig. 9a).

The brown and green amphiboles in the two groups of Hb gabbros are classified as magnesio-hastingsite and magnesio-(ferri) hornblende (^{A}(Na + K + 2Ca) < 0.5 apfu, Fig. 7a−b) respectively, except for two analyses of actinolite (listed in Table S3). The brown amphiboles show variable major element compositions. Compared to the cumulus amphibole in the hornblendite, they display higher MgO (13.7–15.2 wt. %), with lower TiO_2 (0.7−2.0 wt. %) and Al_2O_3 contents (10.6–13.2 wt. %). Although these brown amphiboles also have slightly higher SiO_2 (41.6–44.4 wt. %) than the amphibole in the hornblendite, it does not exceed 45 wt. % (Fig. 8). The chondrite-normalized REE patterns of brown amphiboles in the Hb gabbros are similar to those amphiboles in the hornblendite but more enriched in HREE (Fig. 9b, c).

The green amphiboles in the two groups of gabbros have significantly higher SiO_2 (45.9–50.7 wt. %) but lower TiO_2 (0.3−1.2 wt. %) and Al_2O_3 contents (10.4−4.7 wt. %) than those brown amphiboles. Despite having a broad range, the $Mg^{\#}$ and MgO content of green amphiboles in Group I ($Mg^{\#}$=62–69; MgO=13.4–15.0 wt. %) are generally slightly lower than those in Group II ($Mg^{\#}$=65–72; MgO=13.9–15.9 wt. %) (Fig. 8a, b).

444 This suggests that the two types of green amphiboles formed in different reaction–
445 displacement processes or under different conditions (Xu et al., 2021; Zhu et al., 2024),
446 this will be discussed in more detail in a subsequent section. The chondrite-normalized
447 REE patterns of the green amphiboles are distinctly different from those of the brown
448 amphiboles in the two groups of gabbros. Specifically, the green amphiboles in Group
449 II exhibit right-sloping patterns, whereas those in Group I have significantly lower total
450 REE contents (Fig. 9b, c).Moreover, both green amphiboles have a slight positive Eu
451 anomaly (δEu=1.10−1.56).
452
453 ***Clinopyroxene***
454 Clinopyroxene occurs as a major cumulus phase in the Cpx hornblendite and as
455 small relict inclusions within large brown amphibole in the Group II Hb gabbro. All
456 analyzed grains are diopside in composition with limited variation in Wo content (46–
457 52 mol%) (Fig. 7c). The high Wo content reflects either crystallization in a hydrous arc
458 magma (Wo $>$ 40 mol%; Gaetani et al., 1993; Prouteau & Scaillet, 2003) or
459 crystallization in the absence of orthopyroxene and olivine, which would result in Cpx
460 with a lower Wo content. Clinopyroxene in the Cpx hornblendite has relatively low
461 Mg# (74.9–86.3), with variable concentrations of Al_2O_3 (2.7–5.9 wt. %) and TiO_2
462 (0.26–0.92 wt. %). Their chondrite-normalized REE patterns are hump-shaped with
463 LREE and HREE depletions relative to the MREE, and no Eu anomalies (Fig. 9d). The
464 clinopyroxene relicts in Group II Hb gabbros have higher Mg# (80.0–88.4), but lower
465 Al_2O_3 (0.7–2.9 wt. %) and TiO_2 (0.09–0.26 wt. %) than those in the Cpx hornblendites.

The chondrite-normalized REE patterns show MREE and HREE enrichment and LREE depletion, with significantly lower REE contents than the clinopyroxene in the Cpx hornblendites (Fig. 9d).

Plagioclase

Plagioclase is another dominant mineral in Hb gabbro but is absent in the Cpx hornblendite. Group I Hb gabbros contain minor fresh interstitial plagioclase, which has high Na_2O (10.1−12.5 wt. %), but low CaO (0.12−0.46 wt. %) and K_2O (0.05−0.42 wt. %) contents and ranges from $An_{0.5}$ to $An_{2.1}$ in composition. The plagioclase is characterized by LREE enriched chondrite-normalised patterns, and an unusual negative Eu anomaly (δEu=0.28−0.75, Fig. 9e). Owing to extensive alteration affecting most plagioclase in the Group II Hb gabbros, reliable major element compositions were successfully determined for only three crystals. They have high CaO (14.6−23.9 wt. %), but low Na_2O (0.84−3.95 wt. %) and K_2O (0.3−1.5 wt. %) contents with ranges from An_{64} to An_{93} in composition (Fig. 7d).

5.4 Thermobarometry and Chemometry

Cumulate rocks may not have obvious genetically-related "daughter" felsic counterparts, or even contemporary magmatic assemblages. As such, single-mineral thermobarometry and chemometry is routinely used to reconstruct the crystallization conditions of cumulates, and model their equilibrium melts (e.g. Luo et al., 2024; Nixon et al., 2024). Crystallization conditions of the Zedong cumulate rocks have been

488 determined using multiple thermobarometers formulated for amphibole (Ridolfi, 2021,
489 R21; Higgins et al., 2022, H22; Putirka, 2016, P16; Krawczynski et al. 2012, K12) and
490 clinopyroxene (Higgins et al., 2022; Putirka, 2008, P08; Wang et al., 2021, W21).
491 Determinations of temperature (T), pressure (P), oxygen fugacity (fO_2) and equilibrium
492 melt water content (H_2O_{melt}) are summarized in Supplementary Table 3 (amphibole)
493 and 4 (clinopyroxene).

494 Temperature estimates given by the thermometers used in this study are
495 summarised in Fig. S3a. The P-independent amphibole-only thermometer of P16 gives
496 average temperatures in good agreement with mean R21 and H22. Equilibration
497 temperatures for cumulus amphibole in Cpx hornblendites range from 948 to 995 °C,
498 and brown amphibole grains in two groups of the Hb gabbro range from 924 to 930 °C
499 (I) and 896 to 905 °C (II). The H22, P-dependent (P08 Eq. 32d; Putirka 2008)
500 thermometers and P-independent thermometers (Wang et al., 2021; W21) give mean
501 temperatures of ~1017 to ~1122 °C for cumulus clinopyroxene in Cpx hornblendites
502 and ~1058 to ~1166 °C for relict clinopyroxene in Group II Hb gabbros. Our calculated
503 temperature range broadly matches experimental data, which show that amphibole and
504 clinopyroxene crystallize at 915 – 1000 °C and > 1025 °C in hydrous primitive
505 magmas, respectively (500-800 MPa; Krawczynski et al., 2012).

506 The results obtained from the various barometers applied in this study show a
507 significant range of variation. The pressures calculated using the K12 barometer are
508 markedly higher than those derived from the R21 and H22 barometers (Fig. S3b). To
509 evaluate which barometer yields results that are more geologically realistic, we

510 compiled experimental petrological data on amphibole composition (experimental
511 conditions: 850-1000 °C, starting material: hydrous basalt; data from Putirka (2016)
512 and references therein). We found that the amphibole compositions from this study
513 predominantly fall within the range of experimental data corresponding to pressures of
514 500-800 MPa (Fig. S4). This is particularly evident in the Al^{IV} vs. Al^{VI} plot (Fig. S4a),
515 where amphiboles crystallized under different pressure conditions can be clearly
516 identified, indicating that the Al content in different sites of amphibole is highly
517 sensitive to pressure. In contrast to the R21 barometer, which uses total Al, and the H22
518 barometer, which employs a machine-learning algorithm, the empirical amphibole-only
519 barometer K12 is based on the occupancy of Al at the octahedral site (Al^{VI}) in
520 amphibole. Therefore, the K12 barometer is preferred over R21 and H22. Average
521 pressures estimated by the K12 barometer for cumulus amphibole (669±48 MPa) and
522 brown amphibole (596±65 MPa and 592±55 MPa for Groups I and II Hb gabbro,
523 respectively) are consistent within error. These results are also in good agreement with
524 the experimental data. Furthermore, the hornblendite in this study is plagioclase-free,
525 and plagioclase in the gabbro occurs as an interstitial phase that crystallized later than
526 amphibole. Experimental studies on fractional crystallization indicate that at pressures
527 exceeding ~500 MPa, plagioclase appears very late or is absent in hydrous, calc-
528 alkaline, mantle-derived melts, where clinopyroxene (± orthopyroxene) and amphibole
529 are the dominant liquidus phases (Ulmer, 2007). The absence of magmatic garnet in
530 these cumulates suggests that the crystallization pressure did not exceed 0.8-1 GPa
531 (Alonso-Perez et al., 2008). In conclusion, based on the consistency of the K12

barometer results with experimental data and the supporting mineralogical evidence, we infer that the cumulate rocks in this study formed at mid- to lower-crustal depths.

Single-phase chemometry offers a novel way to estimate the compositions of liquids equilibrated with silicate minerals in cumulates where melt compositions are otherwise inaccessible. The compositions of melts in equilibrium with clinopyroxene calculated using H22 chemometric methods are given in Supplemental Table 4. A series of empirical chemometric equations for calculating the major-element compositions of liquids in equilibrium with amphibole based on an expanded data set of experimental results (Putirka, 2016; Zhang et al., 2017; Humphreys et al., 2019). The calculated major elements are given in Supplemental Table S8. The results calculated using these formulae typically have an associated uncertainty of 10–15% (SiO_2: 3.6-4.1 wt. % (SE); SiO_2: 3.6-4.1 wt. % (SE); TiO_2: 0.59-0.74 wt. % (SE); FeO: 2.0-2.2 wt. % (SE); MgO: 1.12 wt. % (SE); CaO: 1.45 wt. % (SE); K_2O: 0.76 wt. % (SE); Al_2O_3: 1.31 wt. % (SE); Humphreys et al., 2019). The melt Mg# in equilibrium with amphibole and clinopyroxene were calculated following the approach of Putirka (2016), and the Fe–Mg exchange coefficient $K_D(Fe–Mg)^{Apm/Cpx–liquid}$ values in the range 0.28 ± 0.11 and 0.28 ± 0.08 are regarded to be in chemical equilibrium. Partition coefficients for REEs were predicted using the empirical scheme of Humphreys et al. (2019) and Shimizu et al. (2017). These data were then used to calculate the REE compositions of the liquids from which the amphiboles from the Cpx hornblendite and the gabbro crystallized (data see Supplemental Table S9).

6. DISCUSSION

6.1 Post−magmatic Alteration

The presence of epidote, chlorite, and sericite in both two groups of gabbro indicates that they have undergone varying degrees of low-temperature hydrothermal alteration. The green amphiboles may have formed during subsolidus hydrothermal alteration given that some of them occur as replacement rims on the relict clinopyroxene and the brown amphiboles (Fig. 3-4). Since this alteration may have affected the mobility of certain elements, it is crucial to distinguish magmatic amphiboles from amphiboles formed during hydrothermal reaction to ensure a robust interpretation of the subsequent magmatic processes. Given that Ti is a high field strength element, its concentration in low-temperature fluids is extremely low (Coogan, 2003). Olivine and plagioclase (the other reactants in the hydrothermal amphibole–forming reaction) are almost devoid of Ti, therefore any Ti in hydrothermal amphibole must have been derived predominantly from clinopyroxene. The hydrothermal amphibole–forming reaction is commonly accompanied by the formation of iron-titanium oxides that scavenge some Ti, leaving even less for any secondary amphibole. Thus, Ti content in hydrothermal amphiboles must be lower than that in associated clinopyroxene (Coogan, 2003), whereas amphiboles precipitated from late-stage evolved magmas are likely to contain more TiO_2 because of the higher partition coefficient for Ti in amphibole compared to clinopyroxene (Oberti et al., 2000). Our statistical analysis reveals that the Ti content of the green amphibole (TiO_2=0.32−1.16 wt. %) in two groups of gabbro is higher than that of the relict clinopyroxene (TiO_2=0.09−0.26 wt. %), and also exceeds that of most clinopyroxene in the Cpx hornblendites (Fig. S5a-d), therefore favouring

an interpretation of magmatic origin for this amphibole. Moreover, if green amphibole formed through reaction of clinopyroxene (or brown amphibole) with hydrothermal fluids almost devoid of fluid-immobile elements (e.g. Th), it should not contain a higher abundance of Th than its clinopyroxene precursor. However, green amphiboles have a higher Th (0.06–0.28 μg/g) content than clinopyroxene (0.003−0.08 μg/g) and brown amphiboles (0.04–0.07 μg/g) (Fig. S5e-h). This also supports the magmatic nature of green amphiboles (e.g. Wang et al., 2023) because thorium will gradually concentrate in the residual melts during magma evolution as it is highly incompatible in pyroxene and amphibole (Tiepolo et al., 2007).

6.2 Cumulate Origin for Cpx Hornblendite

The Cpx hornblendites, composed entirely of primocrysts of amphibole and clinopyroxene, display typical adcumulate textures (Fig. 3a − c). However, to demonstrate that they formed by direct crystal accumulation, one would generally have to show that the possible cumulus minerals are present in concentrations greater than would be obtained if they had simply crystallized from their parental liquid with no crystal accumulation (Irvine, 1982), or show the presence of late phases that likely crystallized from intracumulus liquid. The SiO_2 content of the melt in equilibrium with cumulate clinopyroxene and amphibole shows that they crystallized from basaltic to andesitic magmas, which contrasts with the ultra−mafic whole-rock compositions of the Cpx hornblendite (Fig. 10a). In addition, the REE abundance and patterns of the whole-rock are similar to those of the amphibole and clinopyroxene themselves (Fig.

9a, d). This indicates that whole-rock compositions of the Cpx hornblendite cannot be the parental liquid of these crystals and are instead cumulate phases that experienced effective crystal-melt separation. Moreover, the higher REE contents (Fig. 9f) of the melt in equilibrium with the cumulate amphibole, compared to the whole-rock of the hornblendite (Fig. 6), provide key evidence for a cumulate origin.

The creation of an adcumulate requires either the removal of the interstitial liquid to bring the primocrysts closer together or post-accumulation growth of the primocrysts from a liquid of constant composition without nucleation of more evolved minerals in the interstitial liquid (Holness, 2021). The former developing during recrystallisation within the crystal pile, with interstitial liquid can be expelled during compaction (Irvine, 1980), but this simplest and most commonly assumed mechanism can largely be discounted (Latypov et al., 2023). In systems in which there is no possibility of crystal accumulation following re-distribution from elsewhere, such as in magmas with relatively high viscosities, cumulates form by in situ nucleation and growth. Thus, the alternative explanation involves nucleation at the temporary top of the crystal pile, following exchange of interstitial liquid with the main body of parent magma by diffusion or convection (Holness, 2021; Latypov et al., 2023). The following microscopic observations and EBSD of fabric analysis suggest that the Cpx hornblendite is more likely to have formed by the second mechanism: (1) Cumulates formed by crystal re-distribution display an abundance of planar grain boundaries formed by the juxtaposition of euhedral mineral grains bounded by growth faces. However, amphibole grains in the Cpx hornblendite have highly irregular shapes, and

620 irregular grain boundaries, do not have any particular orientation relationship with the
621 growth faces of the adjacent crystals. Amphibole and clinopyroxene grains show
622 complex interlocking textures, with partial or complete enclosure by neighboring grains
623 of the same phase (Fig. 3a–c). Such characteristics are typical of in situ growth to
624 impingement, with a continuous nucleation of new grains; (2) crystal transport (such as
625 crystal settling, flotation and magma currents) in cumulates can cause mineral grains to
626 become sorted by size (Holness et al., 2020), potentially leading to a gradation in size.
627 Hydrodynamic sorting may also cause minerals to accumulate in layers based on their
628 density. However, the cumulate rocks in this study showing no modal grading or
629 density-sorting in the field. Moreover, cumulus amphibole and clinopyroxene have a
630 wide range of grain sizes and follow a normal distribution (Fig. 11b), suggesting that
631 these minerals likely formed in situ through prolonged episodes of nucleation in the
632 absence of hydrodynamic sorting; (3) cumulates developed by crystal settling and
633 accumulation commonly display foliation and/or lineation fabrics defined by a
634 preferred orientation of non-equant primocrysts (a shape preferred orientation)
635 (Latypov et al., 2023). The crystallographic preferred orientation of primocrysts
636 (cumulus amphibole and clinopyroxene), as determined by EBSD analysis, is generally
637 weak for all principal axes, notably [010] and [001] (Fig. 11c). This indicates that their
638 formation is unlikely to have involved substantial crystal re-distribution through
639 settling or magmatic flux (e.g. Henry et al., 2021).

640 Cpx hornblendites are characterized by a framework of cumulus clinopyroxene
641 and amphibole grains without other intercumulus minerals (except for minor interstitial

642 amphibole and trace apatite, ＜5 vol. %, Fig. 3a–c). Moreover, the cumulus amphiboles
643 are unzoned and exhibit a consistent and homogeneous composition between the
644 various textural forms (poikilitic and interstitial grains) (Fig. 7－9). Interstitial
645 oikocrysts of amphibole occur between cumulus clinopyroxene and form a single large
646 crystal with all patches being in optical continuity (Fig. 3c). These features suggest that
647 the amphibole crystallized within a buffered system, potentially involving one or more
648 of the following processes: (1) continuous recharge of amphibole-saturated magma; (2)
649 peritectic melt transport through the crystal mush, or (3) complete diffusive re-
650 equilibration (Holness et al., 2021; Nixon et al., 2024). However, petrographic
651 observations indicate that most amphibole in the Cpx hornblendites co-crystallized with
652 clinopyroxene and shows no textural evidence for a peritectic relationship. Although
653 complete diffusive re-equilibration could produce chemical homogeneity, it requires the
654 cumulate pile to remain hot for a sufficiently long duration. The magmatic cooling
655 history argues against this, as the substantial temperature interval ($\Delta T > 100$ °C)
656 between the liquidus crystallization of clinopyroxene and the subsequent appearance of
657 amphibole implies that time for re-equilibration was limited. Furthermore, prolonged
658 high temperatures would be expected to overprint distinctive textural features, yet these
659 features (e.g., irregular shapes, irregular grain boundaries, and grains show complex
660 interlocking) are well-preserved. Collectively, the evidence leads us to favor a model
661 of post-accumulation growth of the primocrysts (from cumulus to poikilitic
662 amphiboles) from a liquid of constant composition. This process occurred without
663 nucleation of more evolved minerals in the interstitial liquid, implying the primocrysts

grew until they impinged on each other. Such a scenario requires open-system behavior, where the interstitial liquid was efficiently exchanged via convection with an overlying melt-rich reservoir (Holness et al., 2021).

6.3 Intercumulus Melt Evolution of Group I Gabbros

The brown amphibole in Group I gabbros show significant compositional variability. Sparsely occurring idiomorphic amphibole grains have major element contents similar to those of the primary amphibole (referring to those amphibole grains in Fig. 8 which overlap with the cumulus amphibole field), suggesting that these represent remnant crystals derived from the Cpx hornblendite. In contrast, amphibole that encloses resorbed clinopyroxene chadacrysts, along with amphibole exhibiting a granoblastic texture, displays higher Mg# and MgO but lower Al_2O_3 and TiO_2 compared to the primary hornblende (Fig. 8). These compositional characteristics, combined with petrographic evidence, indicate that brown amphiboles formed through peritectic reactions consuming the precursor clinopyroxene. This interpretation is further supported by several studies, which demonstrate that a more clinopyroxene-like chemistry relative to primary amphibole is consistent with an origin via peritectic reaction between an evolving melt and earlier-formed clinopyroxene that has high Mg# and low Al_2O_3 and TiO_2 contents (Xu et al., 2021; Zhu et al., 2024). The granoblastic amphibole, in particular, is interpreted as a product of complete reaction-replacement (Smith, 2014; Nixon et al., 2024).

The classic model proposes that cumulate rocks represent mixtures of cumulus

crystals and intercumulus liquid, initially at or close to equilibrium with one another at the liquidus temperature of the parent magma (Wager et al., 1960). If intercumulus liquid is trapped in a closed-system, it solidifies progressively to form post-cumulus overgrowths and interstitial minerals. During this process, the residual liquid becomes increasingly evolved, eventually saturating in phases enriched in incompatible elements (Barnes & Williams, 2024). However, in Group I Hb gabbros, the green amphibole—an early interstitial phase—does not show the expected enrichment in incompatible elements. The significantly lower REE content of the green amphibole relative to the brown amphibole (Fig. 9c) further suggests that the evolving intercumulus liquid was mobile. This is consistent with models indicating that the migration of evolved liquid in a partially open system leads to the loss of incompatible components (Meurer & Meurer, 2006). The escape of intercumulus liquid also removes heat, which is reflected in the temperature difference between the green and brown amphiboles. Thermometric calculations indicate that the brown and green amphiboles crystallized from andesitic to dacitic melts (mean $SiO_2 = 61.7 \pm 1.3$ ($1\sigma_E$) wt. %) at 924–930 °C, and from rhyolitic melts (mean $SiO_2 = 71.4 \pm 1.7$ ($1\sigma_E$) wt. %) at 764–791 °C, respectively (Fig. 10b). Intercumulus plagioclase is always found associated with quartz, and likely represents the latest-stage evolved melt, which is also consistent with the composition of the melt equilibrated with the green amphibole. However, the low-An plagioclase in the late-stage crystallized cumulus phase has an unusual negative Eu anomaly (Fig. 9e). Therefore, it is necessary to discuss the intermediate processes that led to the Eu anomaly in the late-stage evolved melt.

Plagioclase is absent in the Cpx hornblendite with no Eu anomalies (Fig. 6a), suggesting that plagioclase was not involved in the early melt evolution. The absence of plagioclase is ascribed primarily to high H_2O_{melt} and fO_2 in differentiated arc magmas (Fig. 12) similar to other arc-related ultramafic rocks (Nixon et al., 2024). Although the green amphibole exhibits a slight positive Eu anomaly compared to the brown amphibole, and its calculated equilibrated melt shows a corresponding negative Eu anomaly (δEu as low as 0.6; Fig. S6b), the significantly lower δEu values in plagioclase (as low as 0.28) cannot be attributed to green amphibole fractionation. This is due to the high partition coefficient of Eu between plagioclase and felsic melt ($K_D > 1$; Rollinson, 1993). The highly evolved interstitial melt eventually crystallized almost pure albite (very low An content), indicating relatively low melt water content, as water significantly affects Ca–Na partitioning between plagioclase and melt (Sisson & Grove, 1993). This finding is decoupled from the calculated water contents of melts in equilibrium with brown amphibole (6.3–9.1 wt. %) and green amphibole (5.4–7.5 wt. %), suggesting that the evolution of the interstitial melt involved not only melt escape but also fluid exsolution. Studies of seafloor hydrothermal systems worldwide have shown that high-temperature vent fluids often have pronounced positive Eu anomalies (Michard et al., 1983; Michard, 1989). The solubility and mobility of Eu^{2+} are much higher in magmatic-hydrothermal fluids than in silicate melts, and exsolution of high-salinity fluids can lead to extreme negative Eu anomalies (Eu/Eu* as low as 0.01) in the residual melt (Ye et al., 2025). Therefore, we conclude that the intercumulus melt evolution of Group I Gabbros was jointly controlled by melt

730 migration and fluid exsolution.

731

732 ## 6.4 Melt Flush in the Mush: the origin of Group II Gabbros

733 In Group II gabbros, brown amphibole typically contains resorbed clinopyroxene
734 inclusions, with amphibole blebs developing along the cleavage planes of
735 clinopyroxene (Fig. 4a). Some green amphibole occurs as reaction rims surrounding
736 brown amphibole (Fig. 4c), suggesting that both brown and green amphibole formed
737 through peritectic reactions: the brown amphibole resulted from reactions between
738 intercumulus melt and cumulus clinopyroxene, while the green amphibole formed from
739 reactions between the melt and pre-existing brown amphibole. Evidence from mineral
740 reaction textures in mafic-ultramafic cumulates at mid-ocean ridges and arc settings
741 confirms the prevalence of such processes. These textures consistently indicate that the
742 oikocrysts formed through dissolution of the enclosed minerals by intercumulus melt
743 (Smith, 2014; Lissenberg & MacLeod, 2016; Chang et al., 2021; Blundy, 2022;
744 Boulangera & France, 2023; Wang et al., 2023). Compared to the primary cumulus
745 amphibole, brown amphibole has higher SiO_2 content but a nearly constant Mg# (Fig.
746 8a), which can be explained by a reaction that consumes early pyroxene to form
747 amphibole. This reaction suppresses the decrease in the Mg# of the interstitial melt
748 (Klaver et al., 2018). The EPMA mapping of representative amphiboles containing
749 clinopyroxene resorbed inclusions show that green amphibole exhibits lower
750 concentrations of Al and Ti but higher Mg and similar Fe compared to brown amphibole
751 (Fig. 4d). In addition, compared to the green amphibole in the Group I gabbros, which

crystallized directly from an evolved residual melt, the green amphibole in the Group II gabbros has significantly higher Mg# values (Fig. 8). This compositional difference can also be attributed to melt–mush reactions occurring via dissolution–reprecipitation processes, which buffer the composition of the interstitial melt. The melts in equilibrium with both the brown and green amphiboles have relatively constant FeO*/MgO ratios across a range of SiO_2 contents (60–75 wt. %), a characteristic highly consistent with the HPRD suite from Nisyros—a young stratovolcano in the Aegean arc, Greece—but distinct from LPA suites (Fig. 13). The latter evolve rapidly into tholeiitic, peraluminous dacites, as predicted by fractional crystallization (FC) models. In contrast, the HPRD suite from Nisyros represent peritectic boundary liquids extracted from a deep crustal hot zone at the base of a cumulate mush. These liquids formed through reactions in which earlier-generated wehrlite cumulates interacted with melt to produce amphibole (Klaver et al., 2018). Moreover, the occurrence of interstitial calcic plagioclase (with An values up to 90 mol. %; Fig. 7d) and the notably high whole-rock Mg# and MgO values of the Group II gabbros—even exceeding those of the Cpx hornblendites (Fig. 5c−d)—collectively indicate replacements of the more evolved interstitial melt by the more primitive recharge melt leading to reactions (dissolution + precipitation).

This process is remarkably similar to the "melt flush" process proposed by Boulanger & France (2023), which is a novel igneous process where primitive melt recharge replaces evolved interstitial melt in crystal mush, triggering melt-mush reactions and concomitant extraction of the evolved melt to form cumulates. Thus, we

774 use two-stage assimilation-fractional crystallization (AFC) processes to model this melt
775 flush process (Klaver et al., 2018; Wang et al., 2023). The first stage (AFC1) is the
776 assimilation of clinopyroxene and the crystallization of brown amphibole + apatite +
777 plagioclase, and the second stage (AFC2) is the assimilation of brown amphibole and
778 the crystallization of green amphibole + apatite + zircon. We also show the pure FC1
779 and FC2 model which corresponds exactly with the AFC1 and AFC2 models with an
780 assimilated to crystallized mass ratio (r) of zero. Using these assumptions, we calculated
781 the Dy/Yb and La/Sm ratios of melts in equilibrium with brown and green amphibole
782 to compare melt compositions and AFC trends. The D_{REE} values for amphibole were
783 calculated using the parameterized model developed by Humphreys et al. (2019). The
784 D_{REE} values of apatite are the average values determined in experiments (Watson &
785 Green, 1981; Prowatke & Klemme, 2006). Detailed simulation parameters are provided
786 in the caption of Fig. 14 and Table S10. The modeling results show that the AFC1 trends
787 vary insignificantly with r values. In contrast, the assimilant of brown amphibole in the
788 AFC2 model has high REE contents and Dy/Yb ratios. The residual evolving melts
789 show decreasing MREE and HREE contents due to the fractionation of amphibole,
790 apatite, and zircon, and hence they are susceptible to the assimilation of brown
791 amphibole. Therefore, the dissolution of brown amphibole and crystallization of zircon
792 during AFC2 can suppress the decrease in Dy/Yb while promoting an increase in La/Sm
793 of late-stage melt. This observation is consistent with the characteristics displayed by
794 our samples, where a mass ratio of assimilation and crystallization between 0.2 and 0.4
795 can yield the calculated melt compositions for our samples (Fig. 14).

6.5 Evolution of the Zedong Middle−Lower Crustal Magmatic System

A schematic petrological model for the generation of the Zedong hornblende-rich ultramafic–mafic intrusive rocks with chemical and textural heterogeneities is shown in Fig. 15. The mantle-derived primitive magma, after undergoing possible early differentiation (olivine ± clinopyroxene), ascends to the magma reservoir in the middle to lower crust of the Gangdese arc (Fig. 15a − b). Firstly, cotectic clinopyroxene-magnetite-apatite primocrysts crystallized in a relatively high-temperature, high-melt-fraction regime within the magma reservoir and accumulated to form a crystal framework with interstitial melt and heterogeneous permeability (mush zone). The relatively large temperature interval for the crystallization of cumulus clinopyroxene prior to the appearance of postcumulus amphibole allowed for progressive expulsion of interstitial melt during densification of the clinopyroxene framework that promoted by overgrowth and partial compaction. Low-permeability zones can facilitate the formation of cumulate clinopyroxenite at the base of a magma reservoir. The evolved hydrous basaltic-andesitic residual liquids, which were in equilibrium with the cumulus clinopyroxene, migrated upward through the crystal framework. A portion of this liquid cooled and crystallized to form the initial interstitial amphibole (Fig. 15c). In mush layers with high porosity (i.e., high melt fraction), amphibole had sufficient space to develop large euhedral crystals (Fig. 15). When evolved interstitial melt was efficiently expelled and replenished by magmas of similar composition, for instance, within the boundary layers at the interface between

818 the mush and the overlying magma chamber. Amphibole will crystallize in-situ and
819 form overgrowths from a liquid of constant composition without nucleation of more
820 evolved minerals and this requires convective communication with the parent magma.
821 Finally, the amphibole primocrysts grow until they impinge to form the Cpx
822 hornblendite with an adcumulate texture (Fig. 15c, CASE ①).

823 The evolved hydrous melts migrated through the cumulus clinopyroxene crystal
824 framework and not only led to the crystallization of early interstitial brown amphibole,
825 but also triggered dissolution of clinopyroxene and crystallization of brown amphibole
826 via further cooling and peritectic reaction. The accumulation of peritectic melt
827 promoted extensive reaction allowing virtually complete in situ replacement of
828 clinopyroxene by granoblastic amphibole. Diverging from Case ①, a semi-open
829 system formed when the ascending evolved interstitial melt was not replenished. The
830 escape of this melt removed incompatible components, resulting in the late
831 crystallization of incompatible element-depleted green amphibole. The protracted
832 process, driven by the incompatible behavior of water, ultimately led to fluid
833 exsolution. As porosity and permeability gradually decreased, the trapped latest-stage
834 interstitial melt crystallized quartz and albitic plagioclase with an unusual negative Eu
835 anomaly, ultimately forming the Group I Hb gabbros with orthocumulate texture (Fig.
836 15c, CASE ②).

837 If the early clinopyroxene-dominated mush was invaded by genetically unrelated
838 melts before full consolidation, the pre-existing thermal and chemical balance would
839 be broken. Firstly, percolation of an exotic melt triggered partial or complete

dissolution of the clinopyroxene, with concomitant crystallization of brown amphibole along its edges or within its interior. The process was accompanied by the crystallization of plagioclase and apatite, and their subsequent enclosure within the brown amphibole. Following a pulse of magma flushing, the composition of the interstitial melt was substantially modified and equilibrated with the brown amphibole. Subsequently, upon cooling, a peritectic reaction occurred between this melt and the brown amphibole, producing a reaction rim of green amphibole along with interstitial apatite and zircon. The eventual expulsion of the residual interstitial melt ultimately formed the Group II Hb gabbros with cumulate texture (Fig. 15c, CASE ③).

The three types of hornblende-rich cumulate rocks have distinct genetic mechanisms, resulting in differences in texture and composition, which may be related to their formation in different locations within the magma reservoir. The Cpx hornblendite may form in the upper to middle parts of the magma reservoir, where conditions are closer to a liquid−rich parental magma chamber. In contrast, Group I gabbros may form in the mush layer of the lower or margin of the magma reservoir, where porosity and melt permeability are relatively low. Group II gabbros likely formed near the channel of deep magma replenishment into the magma reservoir (Fig. 15b).

6.6 Implications for the Gangdese Arc crustal evolution

Observation of samples and fractional crystallization experiments reveal a mineral fractionation sequence defined by olivine → pyroxene → amphibole + Fe-Ti

862 oxides → plagioclase on H_2O-saturated primary arc magmas at lower crustal
863 conditions (Krawczynski et al., 2012; Ulmer et al., 2018; Guo et al., 2020). The mafic
864 and ultramafic cumulate rocks that can be inferred to form during this fractionation
865 sequence is as follows: dunite → wherlite → pyroxenite → clinopyroxene
866 hornblendite → hornblendite → gabbro. In the Zedong ultramafic-mafic intrusive
867 rocks, neither olivine nor orthopyroxene were observed, however relatively low
868 compatible element (Cr and Ni) contents (Fig. S2e−f) of the Cpx hornblendite
869 indicates likely early olivine and clinopyroxene fractionation. More primitive
870 ultramafic cumulates (such as dunites and pyroxenites) are therefore proposed to occur
871 beneath these hornblende-rich cumulate rocks. The Zedong late Jurassic ultramafic–
872 mafic intrusive rocks define a Z-shaped trend in plot of Mg# vs SiO_2 (Fig. 5d),
873 resembling the cumulate sequence of the Mesozoic Gangdese arc as well as Kohistan
874 arc and Talkeetna arc, and represent the magmatic evolution of an immature arc (Zhu
875 et al., 2022). However, they have more depleted whole-rock Sr–Nd isotopic
876 compositions ($(^{87}Sr/^{86}Sr)_i$ = 0.7040 ~ 0.7046; $\varepsilon_{Nd}(t)$ = +5.4 ~ +6.2) and zircon Hf
877 isotopic compositions (+12.5 to +16.4) in contrast to the cumulates in the lower crust
878 from the Late Cretaceous ($(^{87}Sr/^{86}Sr)_i$ = 0.7043~0.7046; $\varepsilon_{Nd}(t)$ = +2.8 ~ +4.3; $\varepsilon_{Hf}(t)$ =
879 +12.1 ~ +14.1) and the Late Triassic ($(^{87}Sr/^{86}Sr)_i$ = 0.7037~0.7051; $\varepsilon_{Nd}(t)$ = +1.7 ~
880 +5.5; $\varepsilon_{Hf}(t)$ = +0.4 ~ +13.0) Gangdese arc (Fig. S7), indicating that the primitive
881 magma was derived from a more juvenile mantle wedge.

882 Amphibole plays an important role in the petrogenesis and evolution of arc magmas
883 and amphibole-rich mafic–ultramafic rocks are widely found in subduction zones

884 (Cawthorn & O'Hara, 1976; Davidson et al., 2007; Murphy, 2013; Nandedkar et al.,
885 2014), this is because high H_2O contents in mafic arc magmas can cause the early
886 crystallization of pargasitic amphibole and suppress the crystallization of plagioclase
887 (Sisson & Grove, 1993; Grove et al., 2002; Ulmer et al., 2018). Trends of increasing
888 La/Yb and decreasing Dy/Yb with increasing SiO_2 from erupted lavas in modern
889 subduction zones suggest that fractionation of amphibole is widespread (Davidson et
890 al., 2007; Barber et al., 2021). The fractionation of silica-poor and iron-rich amphibole
891 more effectively drives the residual melt compositions toward higher SiO_2 levels,
892 promoting calc-alkaline differentiation trends more efficiently than the fractionation of
893 plagioclase or pyroxene (Davidson et al., 2007; Krawczynski et al., 2012). Melt
894 segregation from an amphibole-dominated mush represents a form of crustal
895 differentiation, which plays a crucial role in the formation of felsic rocks and SiO_2-rich
896 continental crust (Barber et al., 2021).

897 In this study, there are obvious negative correlations between SiO_2 contents and
898 $(Dy/Yb)_N$ ratios among the Late Jurassic basic-ultrabasic intrusive rocks, intermediate-
899 acid intrusive rocks, basalts and andesites within the Zedong area (Fig. 5e). Such a
900 marked geochemical signature has been used to indicate amphibole (±pyroxene and
901 plagioclase) fractionation. Most igneous rocks formed above subduction zones are calc-
902 alkaline and this is thought to be due to the presence of water in the source region
903 (Ducea et al., 2015). Previous experimental studies agree that near liquidus
904 crystallization of amphibole together with Ca-rich pyroxene (Cpx) and olivine at 500–
905 800 MPa can produce calc-alkaline liquids (Anderson 1980; Médard & Grove, 2008;

Krawczynski et al., 2012). The calc-alkaline trend (alkali enrichment, iron depletion) of the Zedong volcanic and granitic suite (Fig. 5b) resulted from amphibole and clinopyroxene fractionation, given that the Cpx hornblendites have the highest $Fe_2O_3^T$ content and their accumulation would lower the residual melt's FeO*/MgO ratio. Calculated melts in equilibrium with the cumulus amphiboles (in the Cpx hornblendite) and brown amphiboles (in the Hb gabbro) overlap the Zedong basaltic andesite and tonalite respectively (Fig. 5 and Fig. S2). In addition, the contemporaneous emplacement (c. 160 Ma) and similar whole-rock isotopic compositions (Fig. S2g), suggest that these lavas and upper crustal granitic rocks may represent the intercumulus melts extracted from cumulates with different amounts of residual amphibole. This indicates that there is a trans-crustal magma plumbing system in the Zedong Late Jurassic arc crust, as described by Cashman et al. (2017).

7. CONCLUSIONS

1. The Zedong mafic-ultramafic intrusive rocks within the central-eastern Gangdese arc mainly consist of the Cpx hornblendite and two groups of Hb gabbro. Zircon U-Pb dating indicates that they were synchronously crystallized at c. 160 Ma.

2. Multiple geobarometers indicate that these intrusions formed in a magma reservoir within the middle to lower crust. The Cpx hornblendite with adcumulate formed through in-situ nucleation and overgrowth at the interface between the mush layer and the convecting parental magma.

3. Group I gabbros with orthocumulate textures formed through the peritectic

reaction between clinopyroxene precursors and evolved interstitial melts, followed by melt migration and fluid exsolution in asemi-open system.

4. The formation of Group II gabbros is associated with a melt flush process relying on melt-mush reactions between the deep recharge melt and crystal mush. The textural and chemical heterogeneities of these hornblende-rich cumulates may be related to their formation at different locations within a common middle−lower crustal magma reservoir.

5. Compared to other periods of the Mesozoic, the Late Jurassic parental arc magma was derived from a more juvenile mantle wedge and records significant growth in the middle−lower crust. Differentiation trends between the cumulate rocks and coeval non-cumulate rocks within the Zedong terrane indicate that the evolution of the Late Jurassic arc crust was mainly controlled by amphibole fractionation.

6. Calculated melts in equilibrium with the cumulus and brown amphiboles overlap the coeval basaltic andesite and tonalite respectively, suggesting the existence of a trans-crustal magma plumbing system.

ACKNOWLEDGEMENTS

We thank the Editor-in-Chief Georg Zellmer, Editor Tod Waight, John Adam, and three anonymous reviewers for their constructive suggestions, which greatly improved the paper. We appreciate the assistance from Yong-Hua Cao, Shan Li and Yi-Chen Zhao during the EPMA and EBSD analysis.

FUNDING

Financial support for this research was provided by the China National Science and Technology Major Project (No. 2024ZD1001103) and the National Natural Science Foundation of China (42021002). This is contribution no. IS-XXXX from GIGCAS.

Data Availability Statement

New geochemical data presented in this study have been deposited in the EarthChem Library at https://ecl.earthchem.org/view.php?id=4299 (DOI: 10.60520/IEDA/114299). The repository templates have been submitted as supplemental materials.

REFERENCES

Aitchison, J. C., Badengzhu, Davis, A. M., Liu, J., Luo, H., Malpas, J. G., McDermid, I. R. C., Wu, H., Ziabrev, S. V. & Zhou, M.−f. (2000). Remnants of a Cretaceous intra−oceanic subduction system within the Yarlung–Zangbo suture (southern Tibet). Earth and Planetary Science Letters 183, 231−244.

Alonso-Perez, R., Müntener, O. & Ulmer, P. (2009). Igneous garnet and amphibole fractionation in the roots of island arcs: experimental constraints on andesitic liquids. Contributions to Mineralogy and Petrology 157, 541-558.

Andersen, T. (2002). Correction of common lead in U–Pb analyses that do not report ^{204}Pb. Chemical Geology 192, 59−79.

Anderson, A. T. (1980). Significance of hornblende in calc−alkaline andesites and basalts. American Mineralogist 65, 837−851.

Barber, N. D., Edmonds, M., Jenner, F., Audétat, A. & Williams, H. (2021). Amphibole control on copper systematics in arcs: Insights from the analysis of global datasets. Geochimica et Cosmochimica Acta 307, 192−211.

Barnes, S. J. & Williams, M. (2024). Postcumulus Processes Recorded in Whole−Rock Geochemistry: a Case Study from the Mirabela Layered Intrusion, Brazil. Journal of Petrology 65, egae019.

Barnes, S. J., Latypov, R., Chistyakova, S., Godel, B. & Schoneveld, L. E. (2021). Idiomorphic oikocrysts of clinopyroxene produced by a peritectic reaction within a solidification front of the Bushveld Complex. Contributions to Mineralogy and Petrology 176, 5.

Best, M. G. (1975). Amphibole-bearing cumulate inclusions, Grand Canyon, Arizona and their bearing on silica-undersaturated hydrous magmas in the upper mantle. Journal of Petrology 16, 212–236.

Blatter, D. L., Sisson, T. W. & Hankins, W. B. (2017). Voluminous arc dacites as

amphibole reaction-boundary liquids. Contributions to Mineralogy and Petrology 172, 1–37.
Blundy, J. (2022). Chemical differentiation by mineralogical buffering in crustal hot zones. Journal of Petrology 63, 1–36.
Boulanger, M. & France, L. (2023). Cumulate Formation and Melt Extraction from Mush−Dominated Magma Reservoirs: The Melt Flush Process Exemplified at Mid−Ocean Ridges. Journal of Petrology 64, egad005.
Burg, J.-P., Arbaret, L., Nawaz Chaudhry, M., Dawood, H., Hussain, S. & Zeilinger, G. (2005). Shear strain localization from the upper mantle to the middle crust of the Kohistan Arc (Pakistan). Geological Society, London, Special Publications 245, 25-38.
Campbell, I. H. (1978). Some problems with the cumulus theory. Lithos 11, 311−323.
Cashman, K. V., Sparks, R. S. J. & Blundy, J. D. (2017). Vertically extensive and unstable magmatic systems: A unified view of igneous processes. Science 355, eaag3055.
Cawthorn, R. & O'Hara, M. (1976). Amphibole fractionation in calc−alkaline magma genesis. American Journal of Science 276, 309−329.
Cawthorn, R. G., Curran, E. B. & Arculus, R. J. (1973). A petrogenetic model for the origin of the calc-alkaline suite of Grenada, Lesser Antilles. Journal of Petrology 14, 327–337.
Chang, J., Audétat, A. & Li, J.−W. (2021). In situ Reaction−replacement Origin of Hornblendites in the Early Cretaceous Laiyuan Complex, North China Craton, and Implications for its Tectono−magmatic Evolution. Journal of Petrology 62.
Conrad, W. K. & Kay, R. W. (1984). Ultramafic and mafic inclusions from Adak Island: crystallization history, and implications for the nature of primary magmas and crustal evolution in the Aleutian Arc. Journal of Petrology 25, 88–125.
Coogan, L. A. (2003). Contaminating the lower crust in the Oman ophiolite. Geology, 31, 1065–1068.
Cooper, G. F., Davidson, J. P. & Blundy, J. D. (2016). Plutonic xenoliths from Martinique, Lesser Antilles: evidence for open system processes and reactive melt flow in island arc crust. Contributions to Mineralogy and Petrology 171, 87.
Costa, F., Dungan, M. A. & Singer, B. S. (2002). Hornblende- and phlogopite-bearing gabbroic xenoliths from Volcan San Pedro (36 S), Chilean Andes: evidence for melt and fluid migration and reactions in subduction-related plutons. Journal of Petrology 43, 219–241.
Daczko, N. R., Piazolo, S., Meek, U., Stuart, C. A. & Elliott, V. (2016). Hornblendite delineates zones of mass transfer through the lower crust. Scientific Reports 6, 31369.
Davidson, J., Turner, S., Handley, H., Macpherson, C. & Dosseto, A. (2007). Amphibole “sponge” in arc crust? Geology 35, 787−790.
DeBari, S., Kay, S. M. & Kay, R. W. (1987). Ultramafic xenoliths from Adagdak

volcano, Adak, Aleutian Islands, Alaska: deformed igneous cumulates from the Moho of an island arc. Journal of Geology 95, 329–341.
Dessimoz, M., Müntener, O. & Ulmer, P. (2012). A case for hornblende dominated fractionation of arc magmas: the Chelan Complex (Washington Cascades). Contributions to Mineralogy and Petrology 163, 567−589.
Ducea, M. N., Saleeby, J. B. & Bergantz, G. (2015). The Architecture, Chemistry, and Evolution of Continental Magmatic Arcs. Annual Review of Earth and Planetary Sciences 43, 299−331.
Foden, J. D. & Green, D. H. (1992). Possible role of amphibole in the origin of andesite: some experimental and natural evidence. Contributions to Mineralogy and Petrology 109, 479–493.
Gaetani, G. A., Grove, T. L. & Bryan, W. B. (1993). The influence of water on the petrogenesis of subductionrelated igneous rocks. Nature 365, 332−334.
Greene, A., DeBari, S., Kelemen, P., Blusztajn, J. & Clift, P. (2006). A Detailed Geochemical Study of Island Arc Crust: the Talkeetna Arc Section, South−Central Alaska. Journal of Petrology 47.
Grimes, C. B., John, B. E., Cheadle, M. J., Mazdab, F. K., Wooden, J. L., Swapp, S. & Schwartz, J. J. (2009). On the occurrence, trace element geochemistry, and crystallization history of zircon from in situ ocean lithosphere. Contributions to Mineralogy and Petrology 158, 757−783.
Grove, T., Parman, S., Bowring, S., Price, R. & Baker, M. (2002). The role of an H_2O−rich fluid component in the generation of primitive basaltic andesites and andesites from the Mt. Shasta region, N California. Contributions to Mineralogy and Petrology 142, 375−396.
Guo, L., Jagoutz, O., Shinevar, W. J. & Zhang, H.−F. (2020). Formation and composition of the Late Cretaceous Gangdese arc lower crust in southern Tibet. Contributions to Mineralogy and Petrology 175, 58.
Helz, R. T. (1973). Phase relations of basalts in their melting range at PH_2O = 5 kb as a function of oxygen fugacity: part I. Mafic phases. Journal of Petrology 14, 249–302.
Henry, H., Kaczmarek, M.-A., Ceuleneer, G., Tilhac, R., Griffin, W. L., O'Reilly, S. Y., Grégoire, M. & Le Sueur, E. (2021). The microstructure of layered ultramafic cumulates: Case study of the Bear Creek intrusion, Trinity ophiolite, California, USA. Lithos 388-389, 106047.
Higgins, M. D. (1991). The origin of laminated and massive anorthosite, Sept Iles layered intrusion, Québec, Canada. Contributions to Mineralogy and Petrology 106, 340-354.
Higgins, O., Sheldrake, T. & Caricchi, L. (2022). Machine learning thermobarometry and chemometry using amphibole and clinopyroxene: a window into the roots of an arc volcano (Mount Liamuiga, Saint Kitts). Contributions to Mineralogy and Petrology 177, 10.
Holloway, J. R. & Burnham, C. W. (1972). Melting relations of basalt with equilibrium water pressure less than total pressure. Journal of Petrology 13, 1–29.

Holness, M. B. (2021). Cumulates and Layered Igneous Rocks. In: Alderton, D. & Elias, S. A. (eds.) Encyclopedia of Geology (Second Edition). Oxford: Academic Press, 99−112.

Holness, M. B., Morris, C., Vukmanovic, Z. & Morgan, D. J. (2020). Insights Into Magma Chamber Processes From the Relationship Between Fabric and Grain Shape in Troctolitic Cumulates. Frontiers in Earth Science Volume 8 - 2020.

Hoskin, P. W. O. & Schaltegger, U. (2003). The Composition of Zircon and Igneous and Metamorphic Petrogenesis. Reviews in Mineralogy and Geochemistry 53, 27−62.

Huang, T.−Y., Wang, Q., Wyman, D. A., Ma, L., Tang, G.−J., Zhang, Z.−P. & Dong, H. (2022). Subduction Erosion Revealed by Late Mesozoic Magmatism in the Gangdese Arc, South Tibet. Geophysical Research Letters 49, e2021GL097360.

Huang, X.−L., Xu, Y.−G., Lo, C.−H., Wang, R.−C. & Lin, C.−Y. (2007). Exsolution lamellae in a clinopyroxene megacryst aggregate from Cenozoic basalt, Leizhou Peninsula, South China: petrography and chemical evolution. Contributions to Mineralogy and Petrology 154, 691−705.

Humphreys, M. C. S., Cooper, G. F., Zhang, J., Loewen, M., Kent, A. J. R., Macpherson, C. G. & Davidson, J. P. (2019). Unravelling the complexity of magma plumbing at Mount St. Helens: a new trace element partitioning scheme for amphibole. Contributions to Mineralogy and Petrology 174, 9.

Irvine, T. N. & Baragar, W. R. A. (1971). A Guide to the Chemical Classification of the Common Volcanic Rocks. Canadian Journal of Earth Sciences 8, 523−548.

Irvine, T. N. (1980). Magmatic density currents and cumulus processes. American Journal of Science 280, 1-58.

Irvine, T. N. (1982). Terminology for Layered Intrusions. Journal of Petrology 23, 127−162.

Jackson, S. E., Pearson, N. J., Griffin, W. L. & Belousova, E. A. (2004). The application of laser ablation−inductively coupled plasma−mass spectrometry to in situ U–Pb zircon geochronology. Chemical Geology 211, 47−69.

Jagoutz, O. & Kelemen, P. B. (2015). Role of Arc Processes in the Formation of Continental Crust. Annual Review of Earth and Planetary Sciences 43, 363-404.

Jagoutz, O., Müntener, O., Schmidt, M. W. & Burg, J.−P. (2011). The roles of flux− and decompression melting and their respective fractionation lines for continental crust formation: Evidence from the Kohistan arc. Earth and Planetary Science Letters 303, 25−36.

Klaver, M., Blundy, J. D. & Vroon, P. Z. (2018). Generation of arc rhyodacites through cumulate−melt reactions in a deep crustal hot zone: Evidence from Nisyros volcano. Earth and Planetary Science Letters 497, 169−180.

Krawczynski, M. J., Grove, T. L. & Behrens, H. (2012). Amphibole stability in primitive arc magmas: effects of temperature, H_2O content, and oxygen fugacity. Contributions to Mineralogy and Petrology 164, 317−339.

Kuno, H. (1968). Differentiation of basalt magmas. In: Hess, H. H. & Poldervaart, A. A. (eds.) Basalts: The Poldervaart Treatise on Rocks of Basaltic Composition. NewYork: Interscience, 623−688.

Larocque, J. & Canil, D. (2010). The role of amphibole in the evolution of arc magmas and crust: the case from the Jurassic Bonanza arc section, Vancouver Island, Canada. Contributions to Mineralogy and Petrology 159, 475−492.

Latypov, R. M., Namur, O., Bai, Y., Barnes, S. J., Chistyakova, S., Holness, M. B., Iacono-Marziano, G., Kruger, W. A. J., O'Driscoll, B., Smith, W. D., Virtanen, V. J., Wang, C. Y., Xing, C. M. & Charlier, B. (2023). Layered intrusions: fundamentals, novel observations and concepts, and controversial issues. Earth-Science Review 249, 104653.

Leake, B. E., Woolley, A. R., Birch, W. D., Gilbert, M. C., Grice, J. D., Hawthorne, F. C., Kato, A., Kisch, H. J., Krivovichev, V. G., Linthout, K., Laird, J., Mandarino, J., Maresch, W. V., Nickel, E. H., Rock, N. M. S., Schumacher, J. C., Smith, D. C., Stephenson, N. C. N., Ungaretti, L., Whittaker, E. J. W. & Youzhi, G. (1997). Nomenclature of amphiboles − Report of the subcommittee on amphiboles of the International Mineralogical Association Commission on New Minerals and Mineral Names. European Journal of Mineralogy 9, 623−651.

Lee, C.-T. A., Cheng, X. & Horodyskyj, U. (2006). The development and refinement of continental arcs by primary basaltic magmatism, garnet pyroxenite accumulation, basaltic recharge and delamination: insights from the Sierra Nevada, California. Contributions to Mineralogy and Petrology 151, 222-242.

Li, W. & Tan, K. (1998). Signal mineral separate method and its significance in geotectonics: taking apatite and zircon as examples. Geotectonica et Metallogenia 22, 83–86.

Li, X. H., Qi, C. S., Liu, Y., Liang, X. R., Tu, X. L., Xie, L. W. & Yang, Y. H. (2005). Petrogenesis of the Neoproterozoic bimodal volcanic rocks along the western margin of the Yangtze Block: New constraints from Hf isotopes and Fe/Mn ratios. Chinese Science Bulletin 50, 2481−2486.

Li, X.−H., Li, Z.−X., Wingate, M. T. D., Chung, S.−L., Liu, Y., Lin, G.−C. & Li, W.−X. (2006). Geochemistry of the 755 Ma Mundine Well dyke swarm, northwestern Australia: Part of a Neoproterozoic mantle superplume beneath Rodinia? Precambrian Research 146, 1−15.

Li, X.−H., Liu, D., Sun, M., Li, W.−X., Liang, X. & Liu, Y. (2004). Precise Sm−Nd and U−Pb isotopic dating of the supergiant Shizhuyuan polymetallic deposit and its host granite, SE China. Geological Magazine − GEOL MAG 141, 225−231.

Lissenberg, C. J. & MacLeod, C. J. (2016). A reactive porous flow control on mid-ocean ridge magmatic evolution. Journal of Petrology, 57(11–12), 2195–2220.

Liu, Y.−S., Gao, S., Hu, Z.−C., Gao, C.−G., Zong, K.−Q. & Wang, D.−B. (2009).

Continental and Oceanic Crust Recycling−induced Melt–Peridotite Interactions in the Trans−North China Orogen: U–Pb Dating, Hf isotopes and trace elements in zircons from mantle xenoliths. Journal of Petrology 51, 537−571.

Locock, A. J. (2014). An Excel spreadsheet to classify chemical analyses of amphiboles following the IMA 2012 recommendations. Computers & Geosciences 62, 1−11.

Ludwig, K. R. (2003). User's Manual for Isoplot/Ex rev. 3.00: A Geochronological Toolkit for Microsoft Excel. Berkeley Geochronology Center Spec. Publ. 4.

Luo, B. J., Ruan, B., Zhang, H. F., Song, J. L., Xu, W. C., Yang, H., et al. (2024). The role of polybaric crystallization in the construction of theGangdese continental magmatic arc, South Tibet. Earth and Planetary Science Letters, 628, 118580.

Ma, L., Wang, Q., Li, Z.−X., Wyman, D. A., Jiang, Z.−Q., Yang, J.−H., Gou, G.−N. & Guo, H.−F. (2013). Early Late Cretaceous (ca. 93 Ma) norites and hornblendites in the Milin area, eastern Gangdese: Lithosphere–asthenosphere interaction during slab roll−back and an insight into early Late Cretaceous (ca. 100–80 Ma) magmatic "flare−up" in southern Lhasa (Tibet). Lithos 172−173, 17−30.

McBirney, A. R. & Noyes, R. M. (1979). Crystallization and Layering of the Skaergaard Intrusion*. Journal of Petrology 20, 487−554.

McBirney. (2007). Igneous Petrology. 3rd ed. Boston: Jones and Bartlett Publisher.

McDermid, I. R. C., Aitchison, J. C., Davis, A. M., Harrison, T. M. & Grove, M. (2002). The Zedong terrane: a Late Jurassic intra−oceanic magmatic arc within the Yarlung–Tsangpo suture zone, southeastern Tibet. Chemical Geology 187, 267−277.

Médard, E. & Grove, T. L. (2008). The effect of H_2O on the olivine liquidus of basaltic melts: experiments and thermodynamic models. Contributions to Mineralogy and Petrology 155, 417−432.

Meurer, W. P. & Meurer, M. E. S. (2006). Using apatite to dispel the "trapped liquid" concept and to understand the loss of interstitial liquid by compaction in mafic cumulates: an example from the Stillwater complex, Montana. Contributions to Mineralogy and Petrology 151, 187–201.

Michard, A. (1989). Rare earth element systematics in hydrothermal fluids. Geochimica et Cosmochimica Acta 53, 745-750.

Michard, A., Albarède, F., Michard, G., Minster, J. F. & Charlou, J. L. (1983). Rare-earth elements and uranium in high-temperature solutions from East Pacific Rise hydrothermal vent field (13 °N). Nature 303, 795-797.

Middlemost, E. A. K. (1994). Naming materials in the magma/igneous rock system. Earth−Science Reviews 37, 215−224.

Morimoto, N. (1988). Nomenclature of Pyroxenes. Mineralogy and Petrology 39, 55−76.

Müntener, O. & Ulmer, P. (2018). Arc crust formation and differentiation constrained by experimental petrology. American Journal of Science 318, 64−89.

Murphy, J. B. (2013). Appinite suites: A record of the role of water in the genesis, transport, emplacement and crystallization of magma. Earth−Science Reviews 119, 35−59.

Namur, O., Charlier, B., Pirard, C., Hermann, J., Liégeois, J.-P. & Auwera, J. V. (2011). Anorthosite formation by plagioclase flotation in ferrobasalt and implications for the lunar crust. Geochimica et Cosmochimica Acta 75, 4998-5018.

Nandedkar, R. H., Ulmer, P. & Müntener, O. (2014). Fractional crystallization of primitive, hydrous arc magmas: an experimental study at 0.7 GPa. Contributions to Mineralogy and Petrology 167, 1015.

Nixon, G. T., Manor, M. J., Scoates, J. S., Spence, D. W. & Milidragovic, D. (2024). Mineralogical constraints on magma storage conditions in ultramafic arc cumulates and the nature and role of cryptic fugitive melts: Tulameen Alaskan−type intrusion, North American Cordillera. Contributions to Mineralogy and Petrology 179, 103.

Oberti, R., Vannucci, R., Zanetti, A., Tiepolo, M. & Brumm, R. C. (2000). A crystal chemical re-evaluation of amphibole/melt and amphibole/clinopyroxene DTi values in petrogenetic studies. American Mineralogist 85, 407-419.

Pan, G. T., Mo, X. X., Hou, Z. Q., Zhu, D. C., Wang, L. Q., Li, G. M., Zhao, Z. D., Geng, Q. R. & Liao, Z. L. (2006). Spatial−temporal framework of the Gangdese Orogenic Belt and its evolution. Acta Petrologica Sinica 22, 521−533.

Peacock, S. M., Rushmer, T. & Thompson, A. B. (1994). Partial melting of subducting oceanic crust. Earth and Planetary Science Letters 121, 227−244.

Perinelli, C., Gaeta, M. & Armienti, P. (2017). Cumulate xenoliths from Mt. Overlord, northern Victoria Land, Antarctica: a window into high pressure storage and differentiation of mantle derived basalts. Lithos 268–271, 225–239.

Prouteau, G. & Scaillet, B. (2003). Experimental Constraints on the Origin of the 1991 Pinatubo Dacite. Journal of Petrology 44, 2203−2241.

Prowatke, S. & Klemme, S. (2006). Trace element partitioning between apatite and silicate melts. Geochimica et Cosmochimica Acta 70, 4513–4527.

Putirka, K. (2016). Special Collection: Rates and Depths of Magma Ascent on Earth: Amphibole thermometers and barometers for igneous systems and some implications for eruption mechanisms of felsic magmas at arc volcanoes. American Mineralogist 101, 841−858.

Putirka, K. D. (2008). Thermometers and Barometers for Volcanic Systems. Reviews in Mineralogy and Geochemistry 69, 61−120.

Rapp, R. P. & Watson, E. B. (1995). Dehydration Melting of Metabasalt at 8–32 kbar: Implications for Continental Growth and Crust−Mantle Recycling. Journal of Petrology 36, 891−931.

Ridolfi, F. (2021). Amp−TB2: An Updated Model for Calcic Amphibole Thermobarometry. Minerals 11:324.

Ridolfi, F., Renzulli, A. & Puerini, M. (2010). Stability and chemical equilibrium of

amphibole in calc-alkaline magmas: an overview, new thermobarometric formulations and application to subduction-related volcanoes. Contributions to Mineralogy and Petrology 160, 45-66.

Rollinson, H. (1993). Using Geochemical Data: Evaluation, Presentation, Interpretation, Reading, MA, Addison-Wesley Longman, p. 352.

Searle, M. P., Windley, B. F., Coward, M. P., Cooper, D. J. W., Rex, A. J., Rex, D., Tingdong, L. I., Xuchang, X., Jan, M. Q., Thakur, V. C. & Kumar, S. (1987). The closing of Tethys and the tectonics of the Himalaya. GSA Bulletin 98, 678−701.

Sen, C. & Dunn, T. (1994). Dehydration melting of a basaltic composition amphibolite at 1.5 and 2.0 GPa: implications for the origin of adakites. Contributions to Mineralogy and Petrology 117, 394−409.

Shimizu, K., Liang, Y., Sun, C., Jackson, C. R. M. & Saal, A. E. (2017). Parameterized lattice strain models for REE partitioning between amphibole and silicate melt. American Mineralogist 102, 2254−2267.

Sisson, T. W. & Grove, T. L. (1993). Experimental investigations of the role of H_2O in calc−alkaline differentiation and subduction zone magmatism. Contributions to Mineralogy and Petrology 113, 143−166.

Sisson, T. W., Ratajeski, K., Hankins, W. B. & Glazner, A. F. (2005). Voluminous granitic magmas from common basaltic sources. Contributions to Mineralogy and Petrology 148, 635−661.

Sláma, J., Kosler, J., Condon, D. J., Crowley, J. L., Gerdes, A., Hanchar, J. M., Horstwood, M. S. A., Morris, G. A., Nasdala, L., Norberg, N., Schaltegger, U., Schoene, B., Tubrett, M. N. & Whitehouse, M. J. (2008). Plesovice zircon - a new natural reference material for U-Pb and Hf isotopic microanalysis. Chemical Geology 249, 1–35.

Smith, D. J. (2014). Clinopyroxene precursors to amphibole sponge in arc crust. Nature Communications 5, 4329.

Sosa, E. S., Bucholz, C. E., Barickman, M. H., VanTongeren, J. A., Setera, J. B., Kay, S. M., & Kay, R. W. (2023). Petrology and geochemistry ofAdak Island plutonic xenoliths: Implications for primitive magma generation and crustal differentiation in the Aleutian Island arc. Journal of Petrology, 64(10), egad073.

Sun, S. S. & McDonough, W. (1989). Chemical and isotopic systematics of oceanic basalts: Implications for mantle composition and processes.

Tiepolo, M., Langone, A., Morishita, T. & Yuhara, M. (2012). On the Recycling of Amphibole−rich Ultramafic Intrusive Rocks in the Arc Crust: Evidence from Shikanoshima Island (Kyushu, Japan). Journal of Petrology 53, 1255−1285.

Tiepolo, M., Oberti, R., Zanetti, A., Vannucci, R. & Foley, S. F. (2007). Trace−Element Partitioning Between Amphibole and Silicate Melt. Reviews in Mineralogy and Geochemistry 67, 417−452.

Tiepolo, M., Tribuzio, R. & Langone, A. (2011). High−Mg Andesite Petrogenesis by Amphibole Crystallization and Ultramafic Crust Assimilation: Evidence from Adamello Hornblendites (Central Alps, Italy). Journal of Petrology 52,

1011−1045.
Ulmer, P. (2007). Differentiation of mantle-derived calc-alkaline magmas at mid to lower crustal levels: experimental and petrologic constraints. Periodico Di Mineralogia 76, 309-325.
Ulmer, P., Kaegi, R. & Müntener, O. (2018). Experimentally Derived Intermediate to Silica−rich Arc Magmas by Fractional and Equilibrium Crystallization at 1.0 GPa: an Evaluation of Phase Relationships, Compositions, Liquid Lines of Descent and Oxygen Fugacity. Journal of Petrology 59, 11−58.
Urann, B. M., Le Roux, V., Jagoutz, O., Müntener, O., Behn, M. D. & Chin, E. J. (2022). High water content of arc magmas recorded in cumulates from subduction zone lower crust. Nature Geoscience 15, 501-508.
Velázquez Santana, L. C., McLeod, C. L., Blakemore, D., Shaulis, B. & Hill, T. (2020). Bolivian hornblendite cumulates: Insights into the depths of Central Andean arc magmatic systems. Lithos 370-371, 105618.
Wager, L. R. & Brown, G. M. (1968). Layered Igneous Rocks. Oliver & Boyd, Edinburgh & London, Edinburgh, 588 pp.
Wager, L. R., Brown, G. M. & Wadsworth, W. J. (1960). Types of Igneous Cumulates. Journal of Petrology 1, 73−85.
Walker, B. A., Bergantz, G. W., Otamendi, J. E., Ducea, M. N. & Cristofolini, E. A. (2015). A MASH zone revealed: The mafic complex of the Sierra Valle Fértil. Journal of Petrology 56, 1863–1896.
Wang, J., Wang, Q., Dan, W., Yang, J.−H., Yang, Z.−Y., Sun, P., Qi, Y. & Hu, W.−L. (2019). The role of clinopyroxene in amphibole fractionation of arc magmas: Evidence from mafic intrusive rocks within the Gangdese arc, southern Tibet. Lithos 338−339, 174−188.
Wang, J., Wang, Q., Sun, P., Dan, W., Kerr, A. C., Zhang, Z.−P., Zhang, L., Wei, G., Dong, H., Hu, W.−L., Yang, Z.−Y., Zhang, X.−Z. & Qi, Y. (2023). Crustal Growth Identified by High−δ18O Zircon and Olivine: A Perspective from Ultramafic Arc Cumulates in Southern Tibet. Journal of Petrology 64, egad052.
Wang, L., Zeng, L., Gao Li, E., Tang, S. & Hu, G. (2012). Remnant Jurassic intra−oceanic arc system in Southern Tibet: Geochemistry and tectonic implications. Acta Petrologica Sinica 28, 1741−1754.
Wang, X., Hou, T., Wang, M., Zhang, C., Zhang, Z., Pan, R., Marxer, F. & Zhang, H. (2021). A new clinopyroxene thermobarometer for mafic to intermediate magmatic systems. Eur. J. Mineral. 33, 621−637.
Watson, E. B. & Green, T. H. (1981). Apatite liquid partitioncoefficients for the rare-earth elements and strontium. Earth and Planetary Science Letters 56, 405–421.
Weis, D., Kieffer, B., Maerschalk, C., Pretorius, W., Barling, J., 2005. High-precision Pb-SrNd-Hf isotopic characterization of USGS BHVO-1 and BHVO-2 reference materials. Geochem. Geophys. Geosyst. 6, 1–10.
Xie, L.−W., Zhang, Y.−B., Zhang, H.−H., Sun, J.−F. & Wu, F.−Y. (2008). In situ simultaneous determination of trace elements, U−Pb and Lu−Hf isotopes in

zircon and baddeleyite. Chinese Science Bulletin 53, 1565−1573.
Xu, W., Zhu, D.−C., Wang, Q., Weinberg, R. F., Wang, R., Li, S.−M., Zhang, L.−L. & Zhao, Z.−D. (2019). Constructing the Early Mesozoic Gangdese crust in Southern Tibet by hornblende−dominated magmatic differentiation. Journal of Petrology 60, 515−552.
Xu, W., Zhu, D.−C., Wang, Q., Weinberg, R. F., Wang, R., Li, S.−M., Zhang, L.−L. & Zhao, Z.−D. (2021). Cumulate mush hybridization by melt invasion: Evidence from compositionally diverse amphiboles in ultramafic–mafic arc cumulates within the eastern Gangdese Batholith, Southern Tibet. Journal of Petrology 62(11), 1-17.
Ye, Z., Tang, M. & Chu, X. (2025). Extreme negative Eu anomalies in peraluminous granites of South China: implications for extensive fluid extraction. Geochimica et Cosmochimica Acta, In Press.
Yoder, H. S. & Tilley, C. E. (1962). Origin of basalt magmas: an experimental study of natural and synthetic rock systems. Journal of Petrology 3, 342–532.
Zhang, J., Humphreys, M. C. S., Cooper, G. F., Davidson, J. P. & Macpherson, C. G. (2017). Magma mush chemistry at subduction zones, revealed by new melt major element inversion from calcic amphiboles. American Mineralogist 102, 1353−1367.
Zhang, L., Ren, Z.−Y., Xia, X.−P., Li, J. & Zhang, Z.−F. (2015). IsotopeMaker: A Matlab program for isotopic data reduction. International Journal of Mass Spectrometry 392, 118−124.
Zhang, L., Ren, Z.−Y., Xia, X.−P., Yang, Q., Hong, L.−B. & Wu, D. (2019). In situ determination of trace elements in melt inclusions using laser ablation inductively coupled plasma sector field mass spectrometry. Rapid Communications in Mass Spectrometry 33, 361−370.
Zhang, L.−L., Liu, C.−Z., Wu, F.−Y., Ji, W.−Q. & Wang, J.−G. (2014). Zedong terrane revisited: An intra−oceanic arc within Neo−Tethys or a part of the Asian active continental margin? Journal of Asian Earth Sciences 80, 34−55.
Zhu, D.−C., Wang, Q., Weinberg, R. F., Cawood, P. A., Chung, S.−L., Zheng, Y.−F., Zhao, Z., Hou, Z.−Q. & Mo, X.−X. (2022). Interplay between oceanic subduction and continental collision in building continental crust. Nature Communications 13, 7141.
Zhu, D.−C., Wang, Q., Weinberg, R. F., Cawood, P. A., Zhao, Z., Hou, Z.−Q. & Mo, X.−X. (2023). Continental crustal growth processes recorded in the Gangdese Batholith, Southern Tibet. Annual Review of Earth and Planetary Sciences 51, 155−188.
Zhu, D.−C., Wang, Q., Zhao, Z.−D., Niu, Y.−L., Hou, Z.−Q., Pan, G.−T. & Mo, X.−X. (2018). Magmatic origin of continental arcs and continental crust formation. Earth Science Frontiers 25, 67−77.
Zhu, D.−C., Zhao, Z.−D., Niu, Y., Mo, X.−X., Chung, S.−L., Hou, Z.−Q., Wang, L.−Q. & Wu, F.−Y. (2011). The Lhasa Terrane: Record of a microcontinent and its histories of drift and growth. Earth and Planetary Science Letters 301, 241−255.

Zhu, R.−Z., Smith, D. J., Wang, F., Qin, J.−F., Zhang, C., Zhao, S., Liu, M., Zhang, F., Zhu, Y. & Lai, S.−C. (2024). Hornblendites as a record of differentiation, metasomatism and magma fertility in arc crust. Chemical Geology 650, 121974.

Figure captions

Figure 1. A geological map of south Tibet showing the tectonic terranes and the location of the Zedong terrane. (a) Tectonic framework of the Tibetan Plateau. Main suture zones: IYZSZ, Indus-Yarlung Zangbo suture zone; BNSZ, Bangong-Nujiang suture zone; LSSZ, Longmu Tso-Shuanghu suture zone; JSZ, Jinshajiang suture zone; AKSZ, A′nemaqin-Kunlun suture zone. (b) The distribution of the Gangdese Batholith and associated volcanic successions (modified after Zhu et al., 2019). LMF, Luobadui-Milashan Fault; SNMZ, Shiquan River-Nam Tso Melange Zone. (c) Simplified sketch map of the central-eastern Gangdese Batholith showing the locations of the Zedong terrane (modified from the latest Zedong 1:50000 geological mapping (2019)).

Figure 2. Field photographs of typical mafic-ultramafic intrusive rocks from the Zedong terrane. (a) and (b) Field relationship between Cpx hornblendite and two Groups of Hb gabbro. (c) Coarse-grained and (d) medium- to fine-grained Cpx hornblendite. (e) Typical appearance of Group I Hb gabbro. (f) Typical appearance of Group II Hb gabbro.

Figure 3. Representative photomicrographs of mafic-ultramafic intrusive rocks from the Zedong terrane. (a−c) Cpx hornblendite. (d−f) Group I Hb gabbro. Note that (b) and (f) are under cross-polarized light and others are under plane-polarized light. C−Amp,

cumulus amphibole; p−Amp, poikilitic amphibole; i−Amp, interstitial amphibole; b−Amp, brown amphibole; g−Amp, green amphibole; c−Cpx, cumulus clinopyroxene; r−Cpx, relict clinopyroxene; Mag, magnetite; Ap, apatite; Pl, plagioclase; Qz, quartz. (See text for detailed descriptions)

Figure 4. (a-c) Representative photomicrographs the Group II Hb gabbro. (b) corresponds to the region enclosed by the yellow box in (a). Note that (b) is Backscattered electron (BSE) image. (d) BSE image and EPMA elemental X-ray maps of one selected representative amphibole containing clinopyroxene resorbed inclusions.

Figure 5. Whole-rock major and trace element compositions of the Zedong ultramafic-mafic cumulate rocks and coeval non-cumulate rocks. (a) $Na_2O + K_2O$ (wt. %) vs SiO_2 (wt. %) (TAS) diagram (Middlemost, 1994). (b) AFM diagram with discriminatory lines of Irvine & Baragar (1971) and Kuno (1968) classifying the calc-alkaline and tholeiitic magmatic series. (c) Whole-rock MgO (wt. %) vs. SiO_2 (wt. %) plot. (d) Whole-rock Mg# vs. SiO_2 (wt. %) plot (modified after Zhu et al. (2022)). Z-shaped trend of Kohistan (dashed red line) and Talkeetna (dashed green line) are according to Jagoutz et al. (2011) and Müntener & Ulmer (2018). (e) Whole-rock $(Dy/Yb)_N$ vs. SiO_2 (wt. %) plot (subscript N denotes normalized to the chondrite values of Sun & McDonough (1989)). (f) Whole-rock total Fe_2O_3 (wt. %) vs. SiO_2 (wt. %) plot. Mg# = molar $Mg/(Mg+Fe^{2+})$. Data for cumulate rocks, volcanic rocks and granitic rocks from Huang et al. (2022), Wang et al. (2012) and Zhang et al. (2014). Error bars in (c), (d), and (f) show

uncertainty of major element compositions from calculated melt equilibrium with amphibole (datas see Supplementary Table S8).

Figure 6. Chondrite-normalized REE patterns and primitive-mantle-normalized trace element patterns for the mafic-ultramafic intrusive rocks from the Zedong terrane. Chondrite and primitive mantle values from Sun & McDonough (1989). Data for cumulate rocks, volcanic rocks and granitic rocks from Zhang et al. (2014).

Figure 7. Mineral compositions of representative amphibole, clinopyroxene and plagioclase for the mafic-ultramafic intrusive rocks from the Zedong terrane. (a) and (b) Classification of amphibole according to the nomenclature of Leake et al. (1997) as follows: $Ca_B \geqslant 1.50$; $(Na+K)_A \geqslant 0.50$; $Ti < 0.50$ and $Ca_B \geqslant 1.50$; $(Na+K)_A < 0.50$; $Ca_A < 0.50$, respectively. (c) Data for clinopyroxene plotted on the enstatite-ferrosilite-diopside-hedenbergite quadrilateral of Morimoto (1988). (d) Classification of plagioclase.

Figure 8. SiO_2, MgO, TiO_2 and Al_2O_3 variations vs. Mg# of amphibole. Mg# $=Mg/(Mg+Fe^{Tot})$.

Figure 9. Chondrite-normalized rare earth element patterns for amphibole (a−c), clinopyroxene (d), plagioclase (e), and liquids in equilibrium with cumulus amphibole (f). Normalization values are from Sun & McDonough (1989).

Figure 10. (a) The variations in Mg# and SiO_2 (wt. %) of the calculated melts in equilibrium with amphibole. (b) The variations in equilibration temperatures and SiO_2 (wt. %) of the calculated melts in equilibrium with amphibole. The melt SiO_2 contents in equilibrium with amphibole and clinopyroxene were calculated using P16 (Putirka, 2016) and H21 (Higgins et al., 2021), respectively. The melt Mg# in equilibrium with amphibole and clinopyroxene were calculated following the approach of Putirka (2016), and the Fe–Mg exchange coefficient $K_D(Fe–Mg)^{Apm/Cpx–liquid}$ values in the range 0.28 ± 0.11 and 0.28 ± 0.08 are regarded to be in chemical equilibrium. Error bars show uncertainty of major element compositions from calculated melt equilibrium with amphibole.

Figure 11. EBSD results of the Cpx hornblendite (sample 09TB01-2). (a) EBSD-derived phase map showing the range of microstructures observed in the Cpx hornblendite; (b) Histogram of the grain sizes (hornblende and clinopyroxene) calculated using EBSD data; (c) Crystallographic preferred orientation of hornblende and clinopyroxene in the Cpx hornblendite.

Figure 12. Hygrometry and oxygen fugacity results for amphiboles from the studied ultramafic-mafic cumulate of the Zedong intrusion. Calculated following the approach

of Ridolfi et al. (2010) and Putirka (2016).

Figure 13. FeO^T/MgO vs. SiO_2 for equilibrium melts of Amp from hornblendite and Group II gabbro (modified after Klaver et al. (2018)). Calculating following the approach of Putirka (2016) and Humphreys et al. (2019). Error bars show uncertainty of major element compositions from calculated melt equilibrium with amphibole.

Figure 14. Geochemical models reproducing the variations in Dy/Yb and La/Sm ratios of the calculated melts in equilibrium with amphibole in the Cpx hornblendite and Group II Hb gabbro. The AFC1 and AFC2 models assume the following peritectic reactions: $Melt_1$ + Cpx = $Melt_2$ + 0.75 Brown Amp + 0.20 Pl + 0.05 Ap (r = 0.4); $Melt_2$ + Brown Amp = $Melt_3$ + 0.9 Green Amp + 0.095 Ap + 0.005 Zrn (r = 0.2 − 0.4). REE partition coefficients for amphibole are calculated using the parameterized models developed by Humphreys et al. (2019). $Melt_1$ is the most primitive basalt reported in the Zedong area (data from Zhang et al. (2014)). The proportions of the assimilated and crystallized minerals are based on the modal mineral proportions in thin sections. The pure FC1 and FC2 models correspond exactly with the AFC1 and AFC2 models with r = 0, respectively. Nodes on the modeled curves indicate 10% changes in the fraction of melt remaining.

Figure 15. (a) Formation of (ultra)mafic cumulates in the middle−lower crust dominated by fractional crystallization of primitive arc magma during oceanic

subduction. (b) Schematic diagram of the middle−lower crustal magma reservoir and the hornblende-rich cumulates with textural and chemical heterogeneities generated at different locations. (c) Schematic petrological model for the generation of the Zedong hornblende-rich ultramafic–mafic intrusive rocks.

Figure S1. LA-ICP-MS zircon U-Pb concordia diagrams for the Hb gabbro sample 09TB143 from the Zedong terrane along with representative zircon CL images. Red circles denote the analytical spots used for U-Pb dating.

Figure S2. Variation diagrams of major elements (wt. %) and selected trace elements (μg/g) vs SiO_2 (wt. %) for the mafic-ultramafic intrusive rocks from the Zedong terrane. N denotes normalized to the chondrite values of Sun & McDonough (1989).

Figure S3. Comparison of equilibration temperatures (a) and pressure (b) for amphibole and clinopyroxene in the Cpx hornblendite and two groups of gabbro as determined by the different amphibole- and clinopyroxene-only thermobarometers used in this study. Error bars indicate the 1σE uncertainties for the models. R21, Ridolfi, 2021; P08, Putirka, 2008; K12, Krawczynski et al., 2012; P16, Putirka 2016; H22, Higgins et al. 2022; W21, Wang et al., 2021.

Figure S4. Comparison between the amphibole compositions from this study and experimental petrological data on amphibole composition (experimental conditions:

850−1000 °C, starting material: hydrous basalt; data from Putirka (2016) and references therein).

Figure S5. Histograms of TiO_2 and Th contents in amphibole and clinopyroxene from the Zedong mafic-ultramafic rocks.

Figure S6. (a) δEu vs. La/Sm of amphibole. (b) δEu vs. La/Sm of the calculated melts in equilibrium with amphibole. The melt REE contents in equilibrium with amphibole were calculated using Humphreys et al. (2019).

Figure S7. Variation of whole-rock $(^{87}Sr/^{86}Sr)_i$ vs. whole-rock $\varepsilon_{Nd}(t)$ (a) and zircon $\varepsilon_{Hf}(t)$ vs. age (Ma) (b) for the Mesozoic (200–90 Ma) hornblende-rich mafic-ultramafic intrusive rocks within the southern Lhasa subterrane. Data source: Late Triassic from Xu et al. (2019); Late Jurassic from this study and Zhang et al. (2014); Late Cretaceous from Guo et al. (2020).

1532 **Fig. 1.**

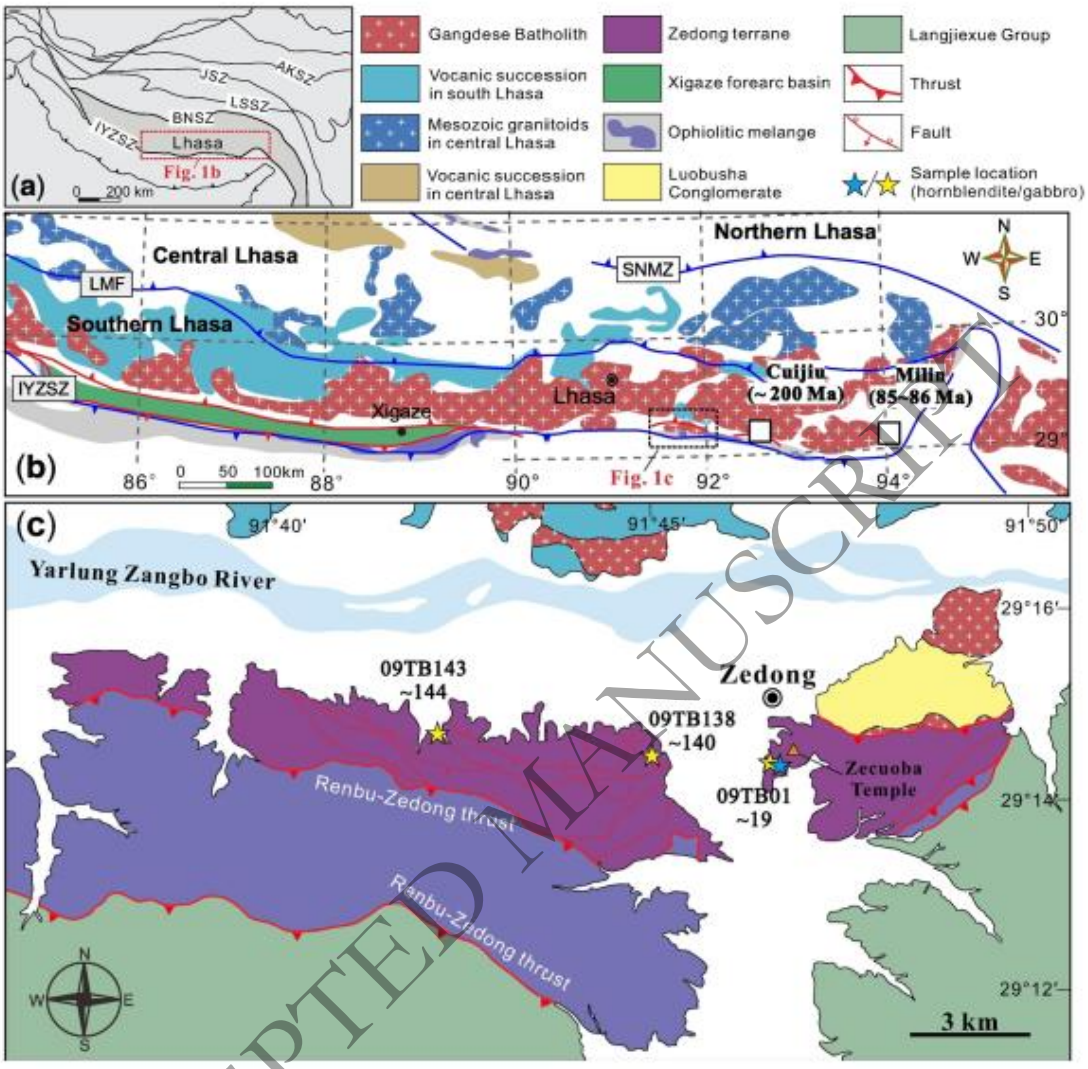

1533

1534

1535 **Fig. 2.**

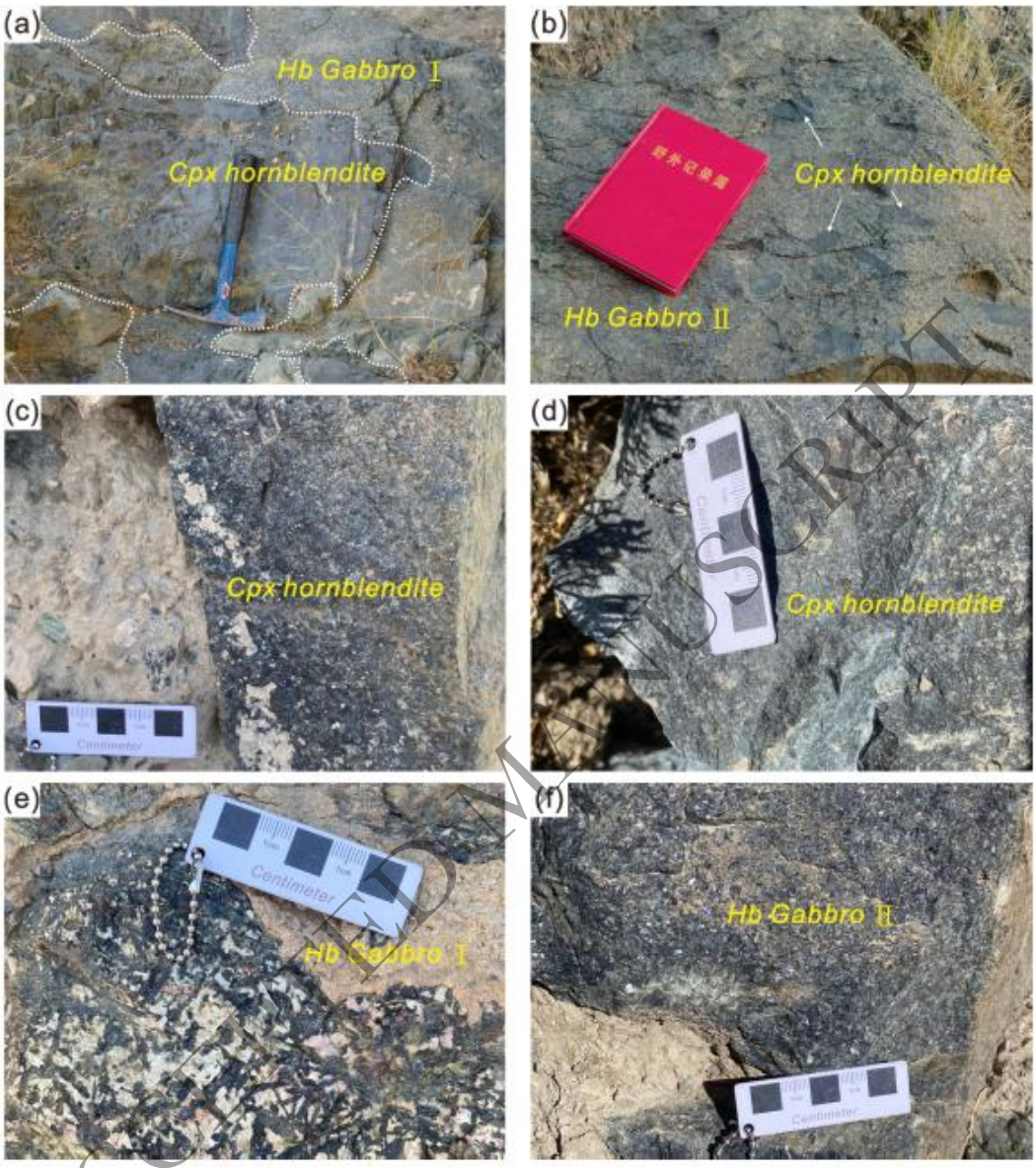

1536

1537

1538 **Fig. 3.**

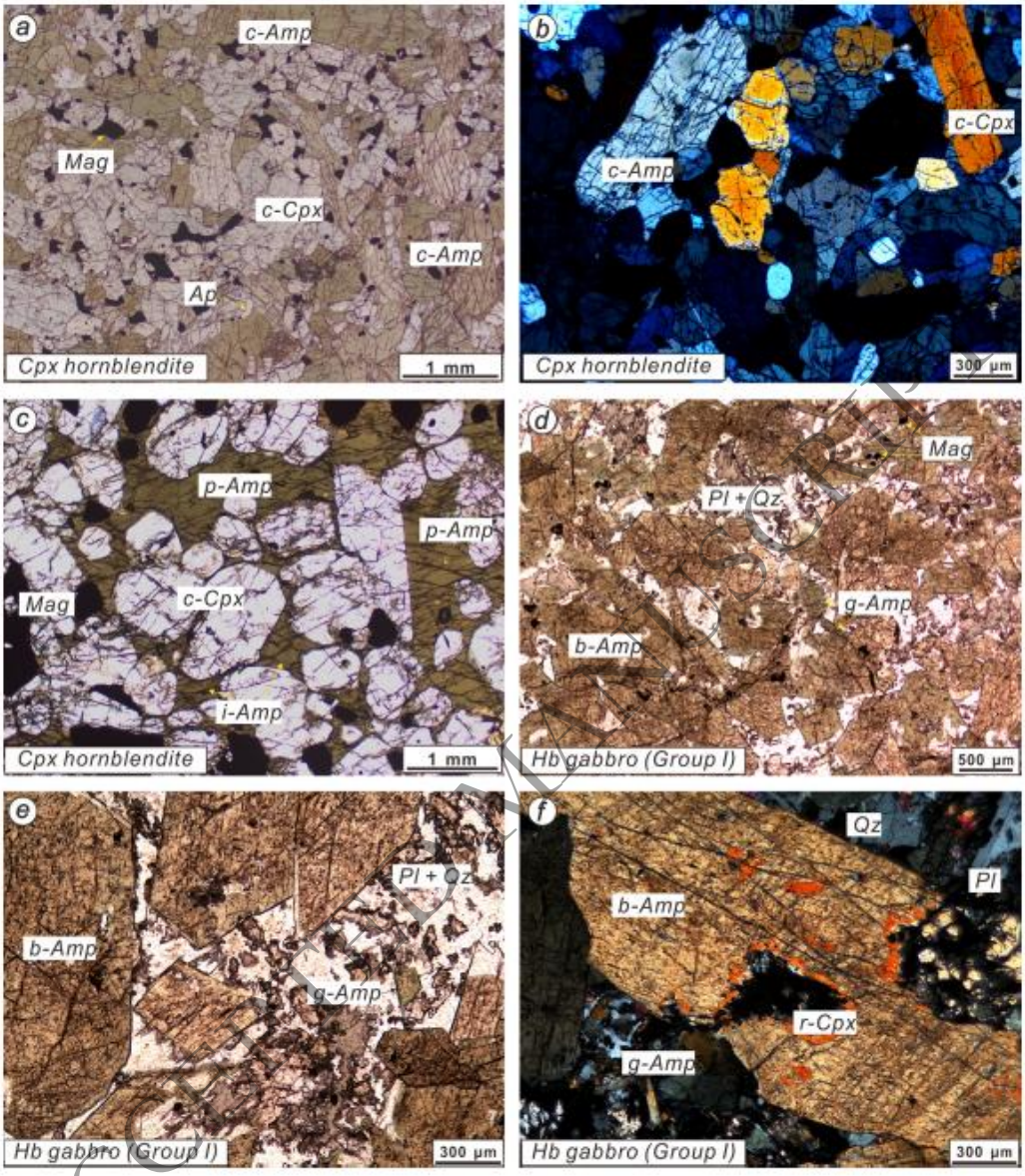

1539
1540

1541 **Fig. 4.**

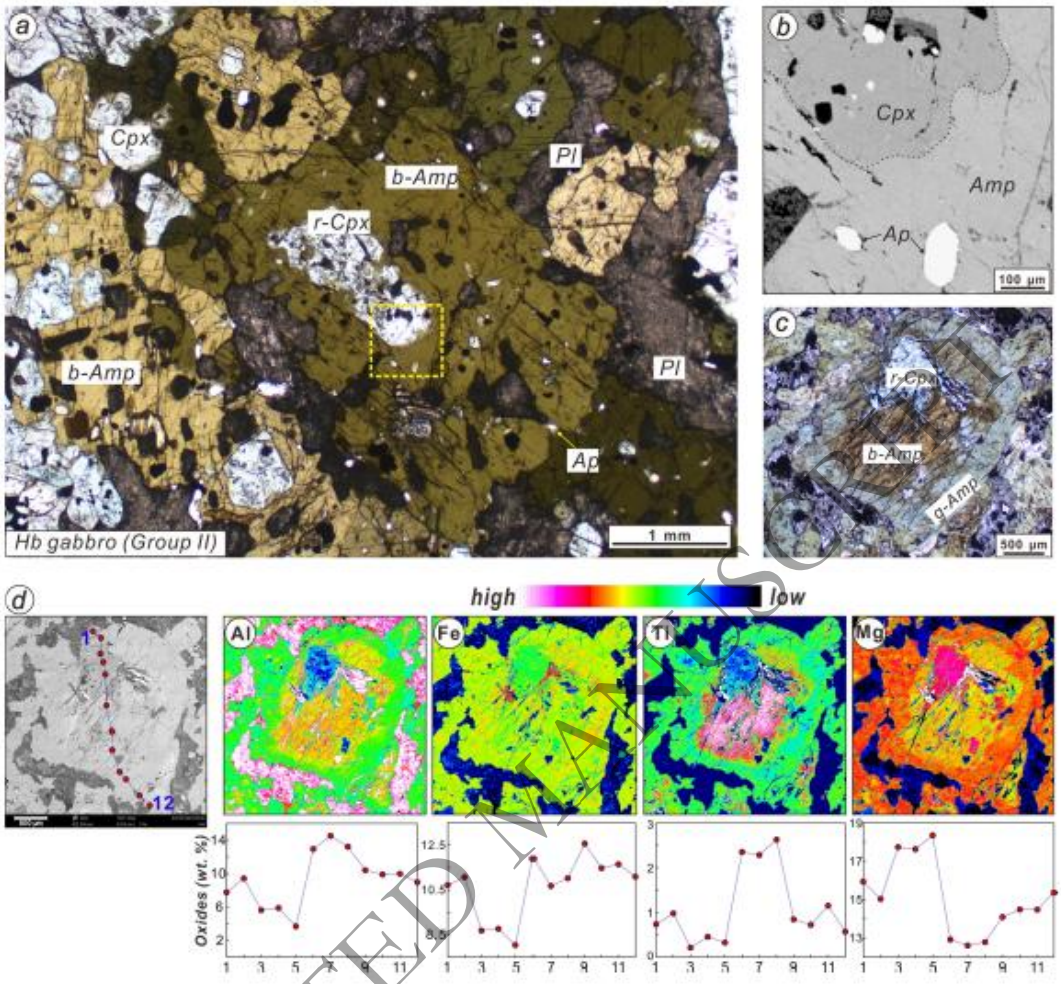

1542

1543

1544 **Fig. 5.**

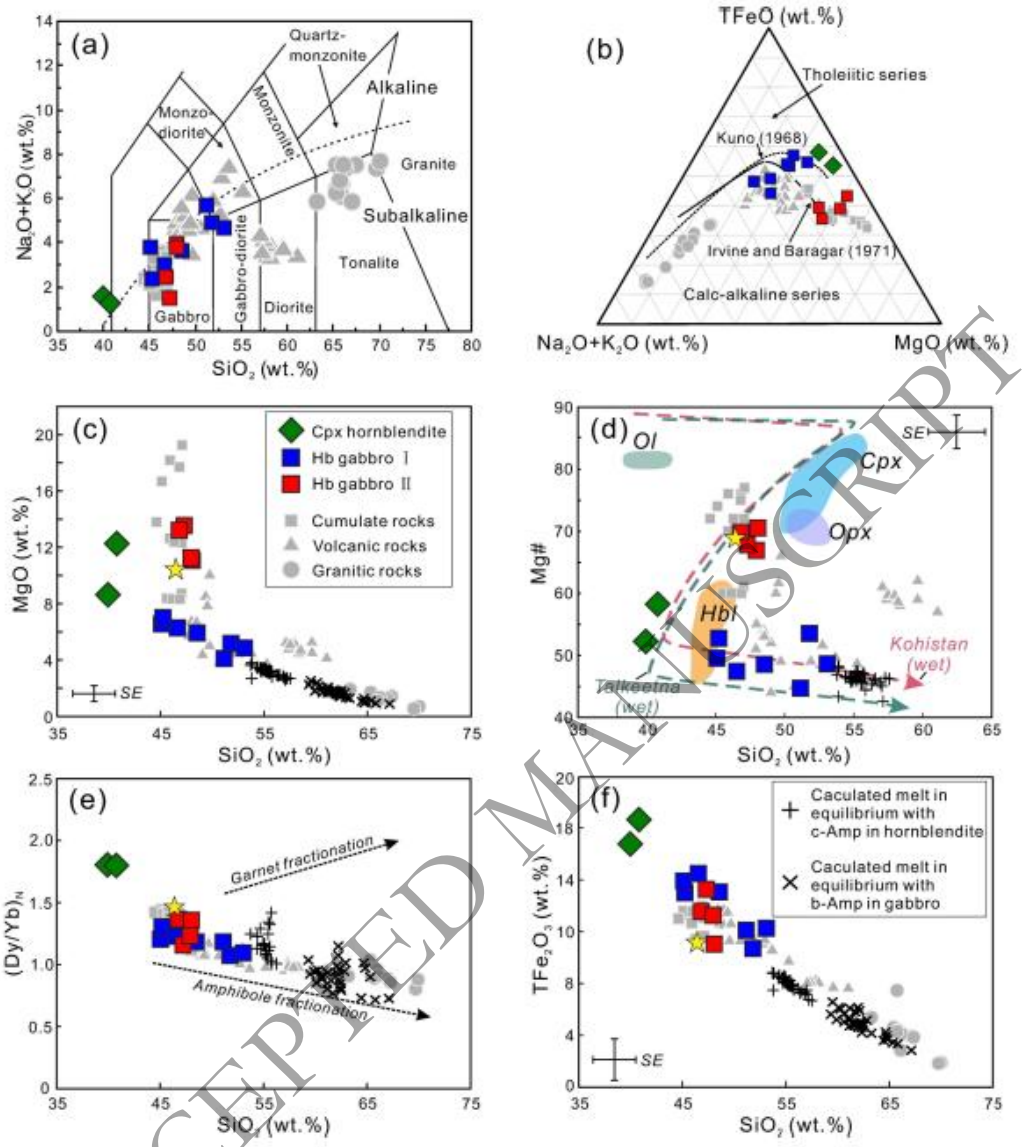

1545

1546

1547 **Fig. 6.**

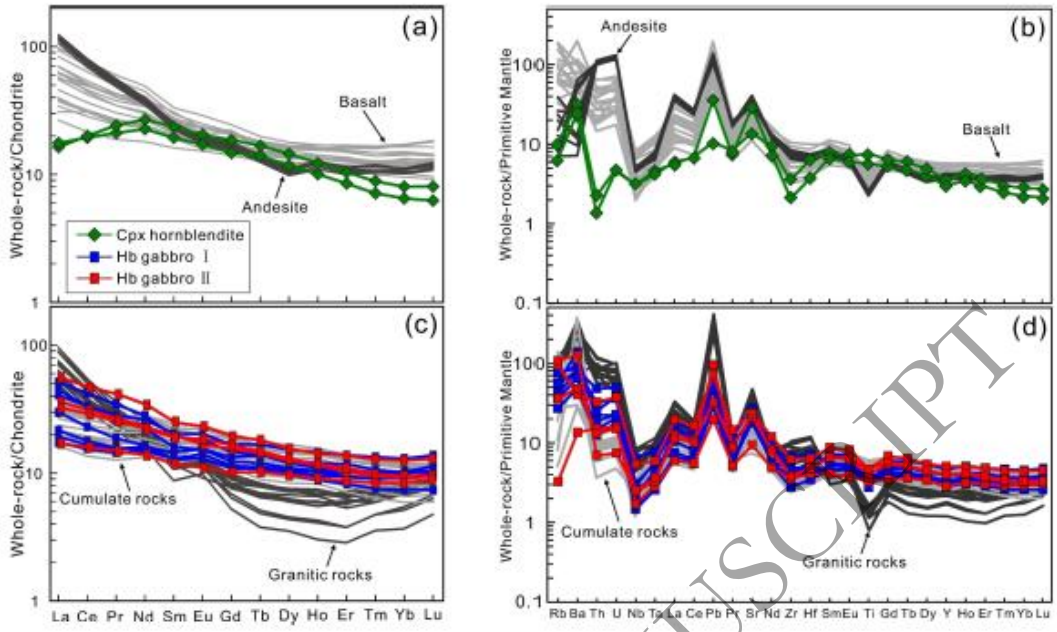

1548

1549

1550 **Fig. 7.**

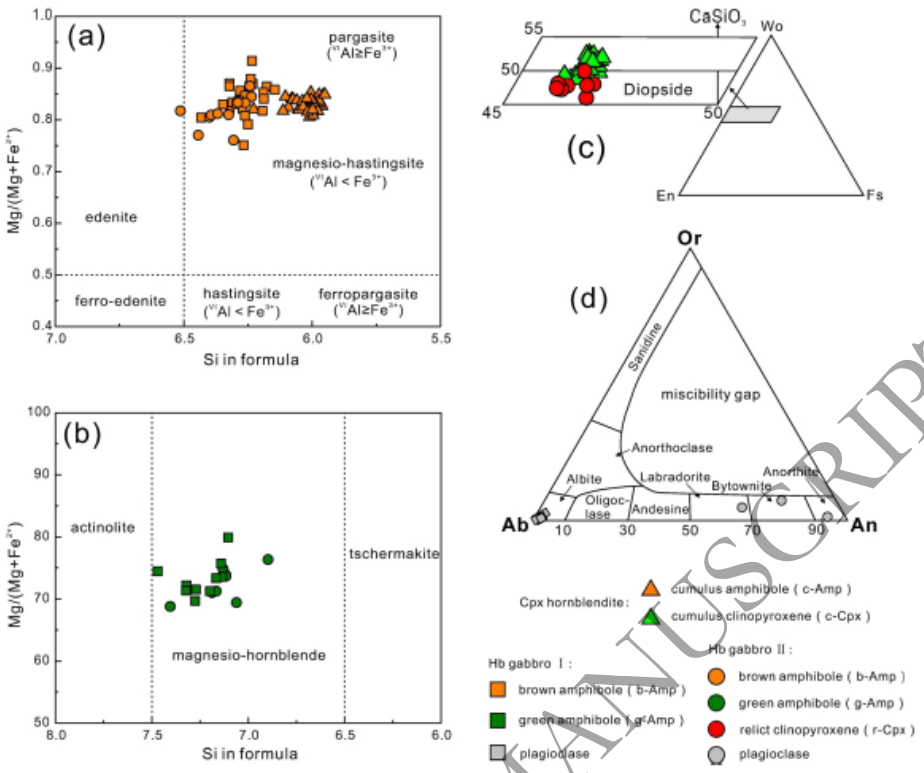

1551

1552

1553 **Fig. 8.**

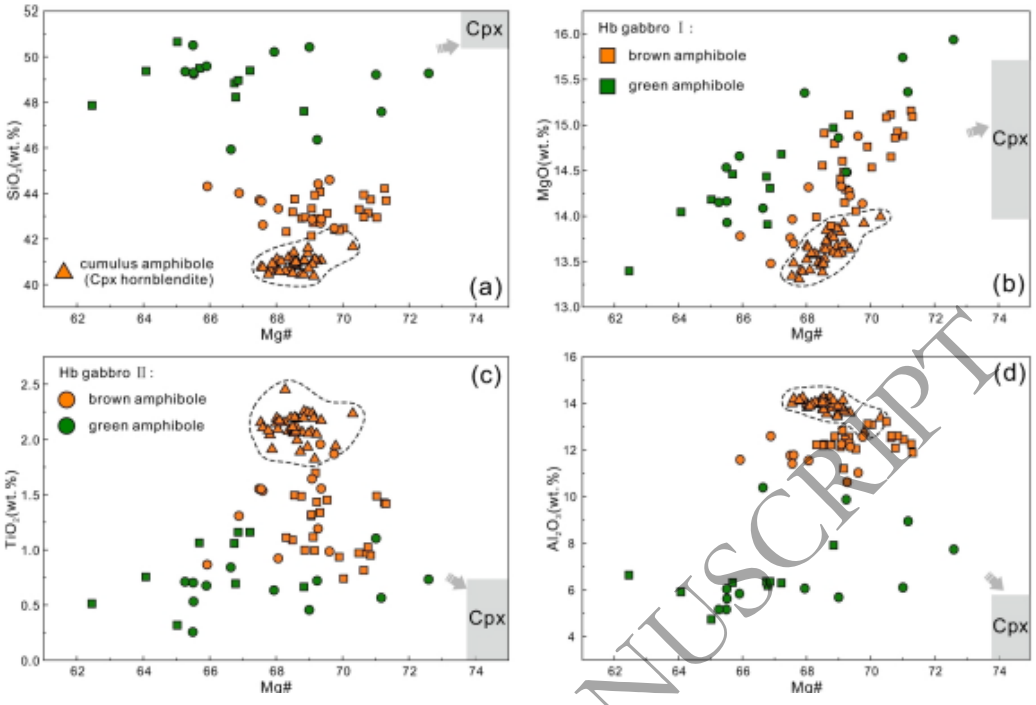

1554

1555

1556 **Fig. 9.**

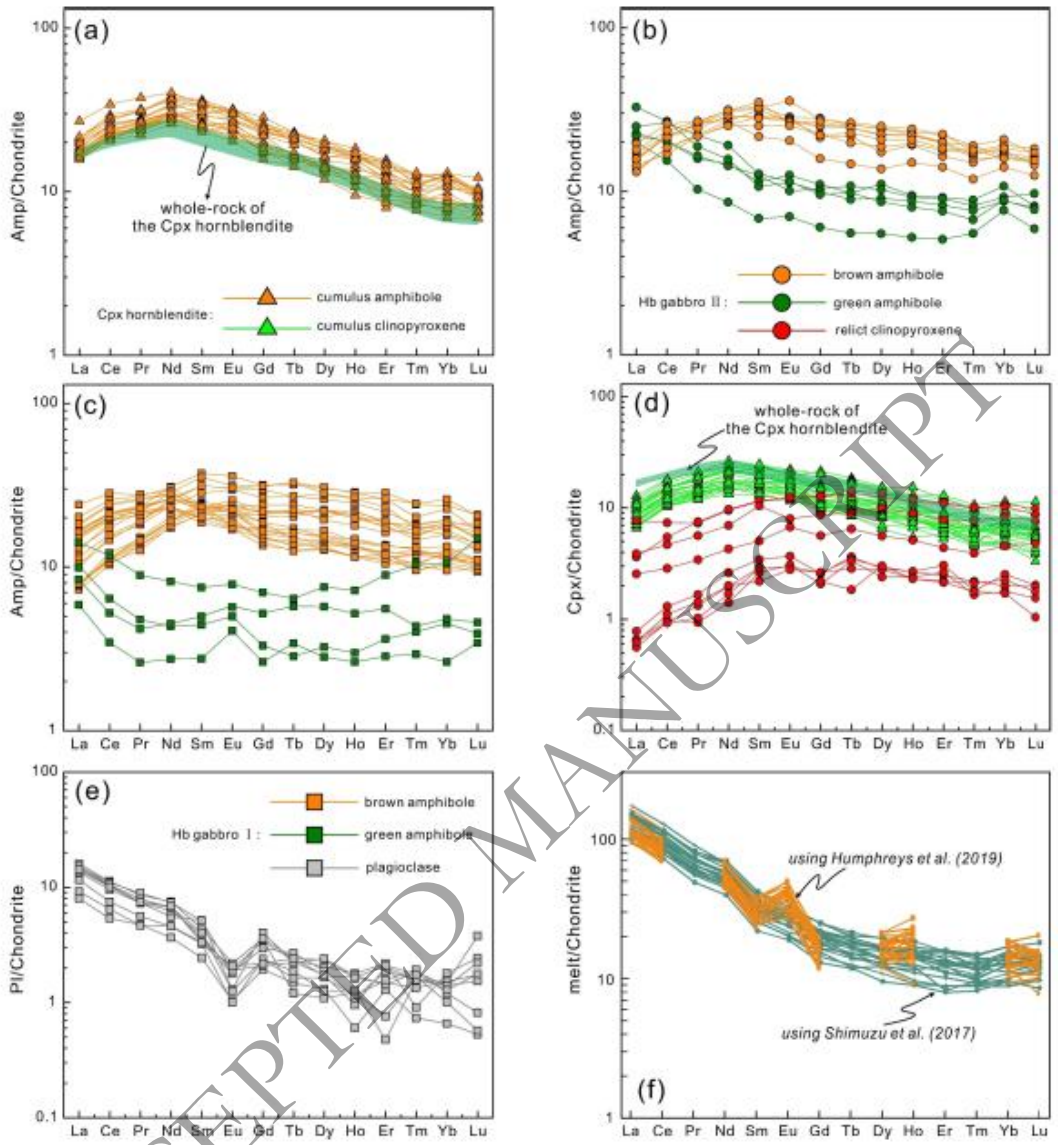

1557

1558

1559

1560 **Fig. 10.**

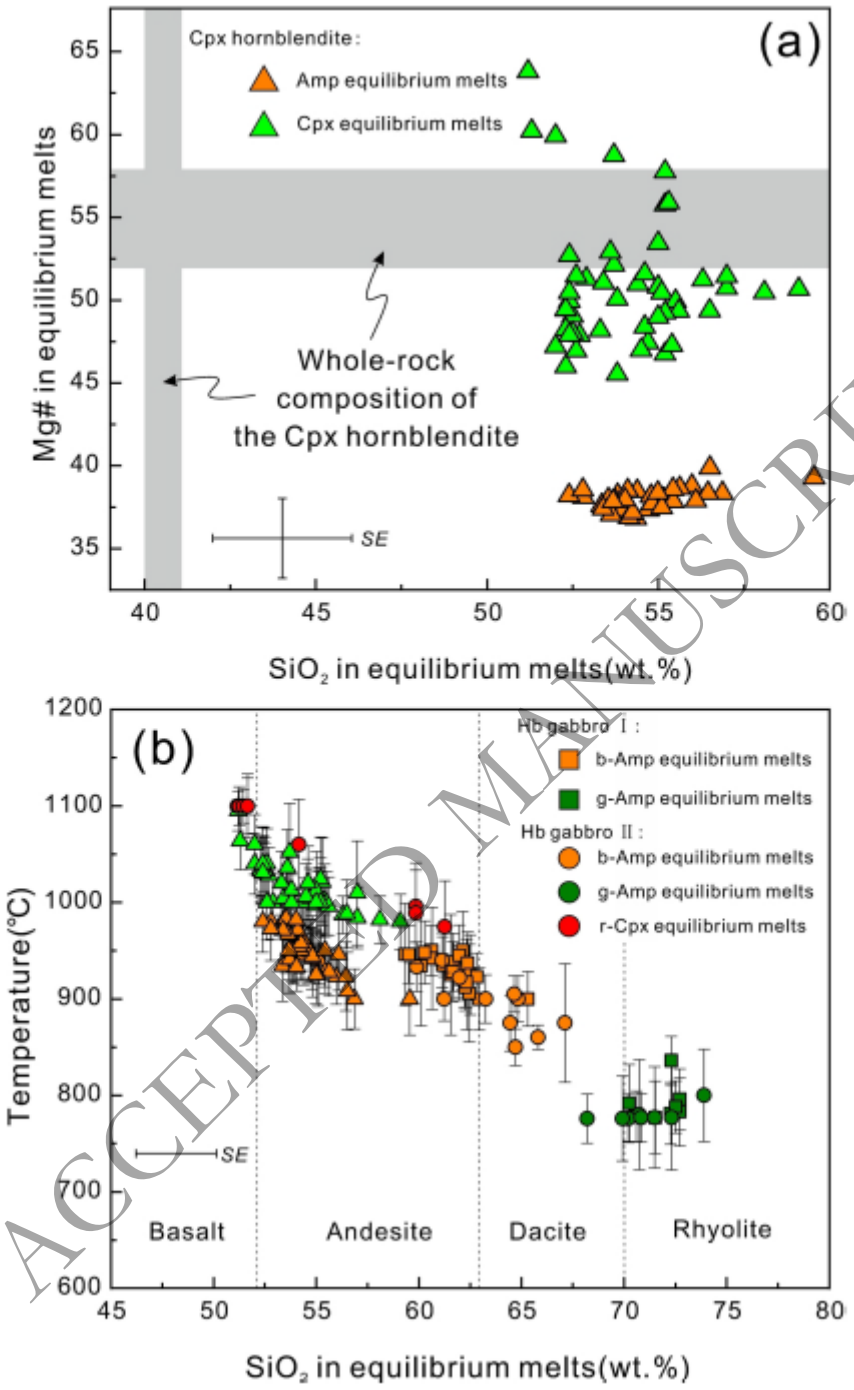

1561

1562

1563

1564

1565 **Fig. 11.**

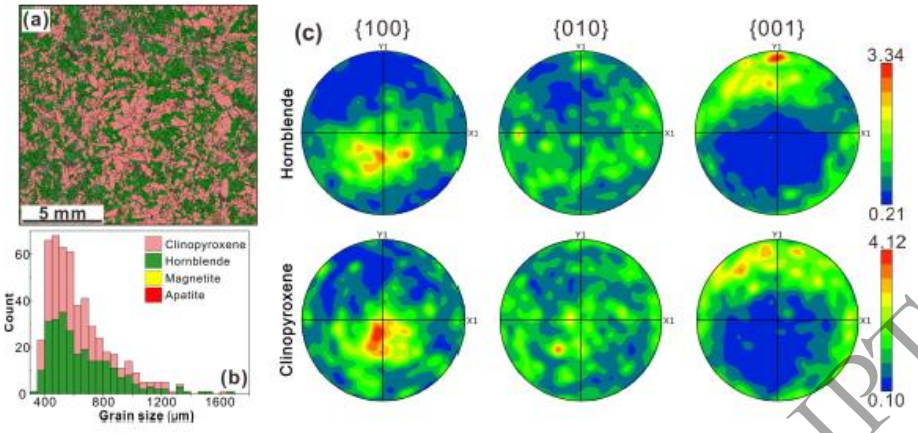

1566

1567

1568

1569 **Fig. 12.**

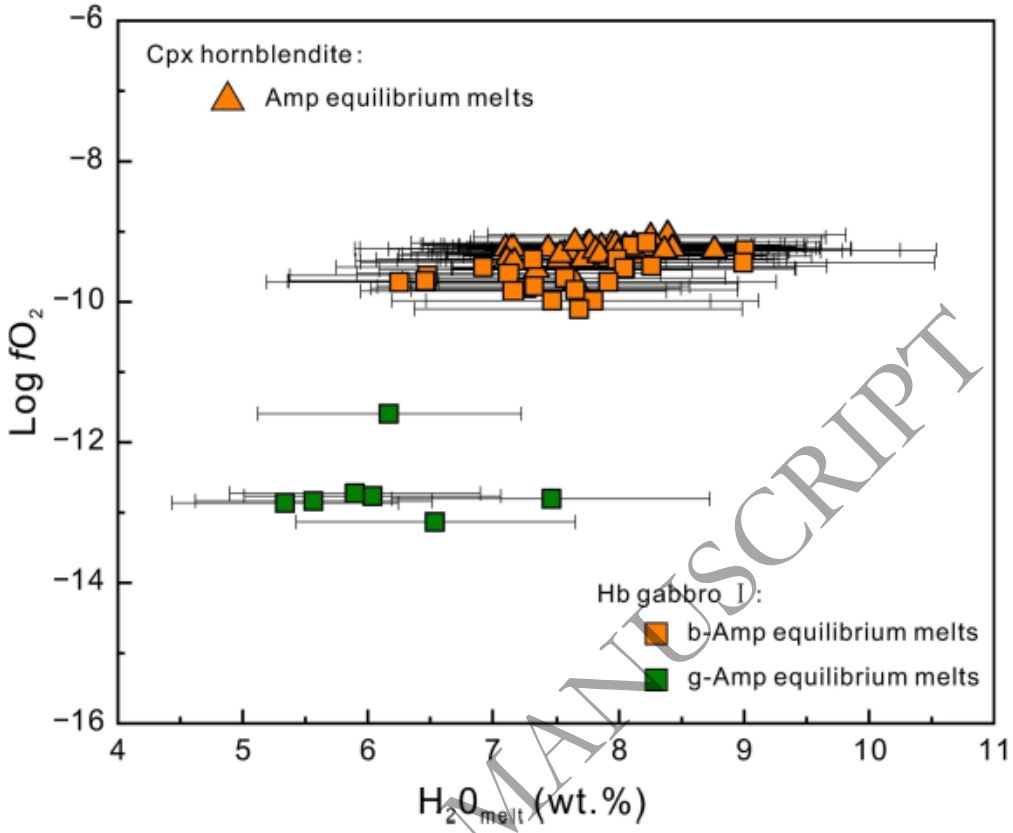

1570
1571

1572 **Fig. 13.**

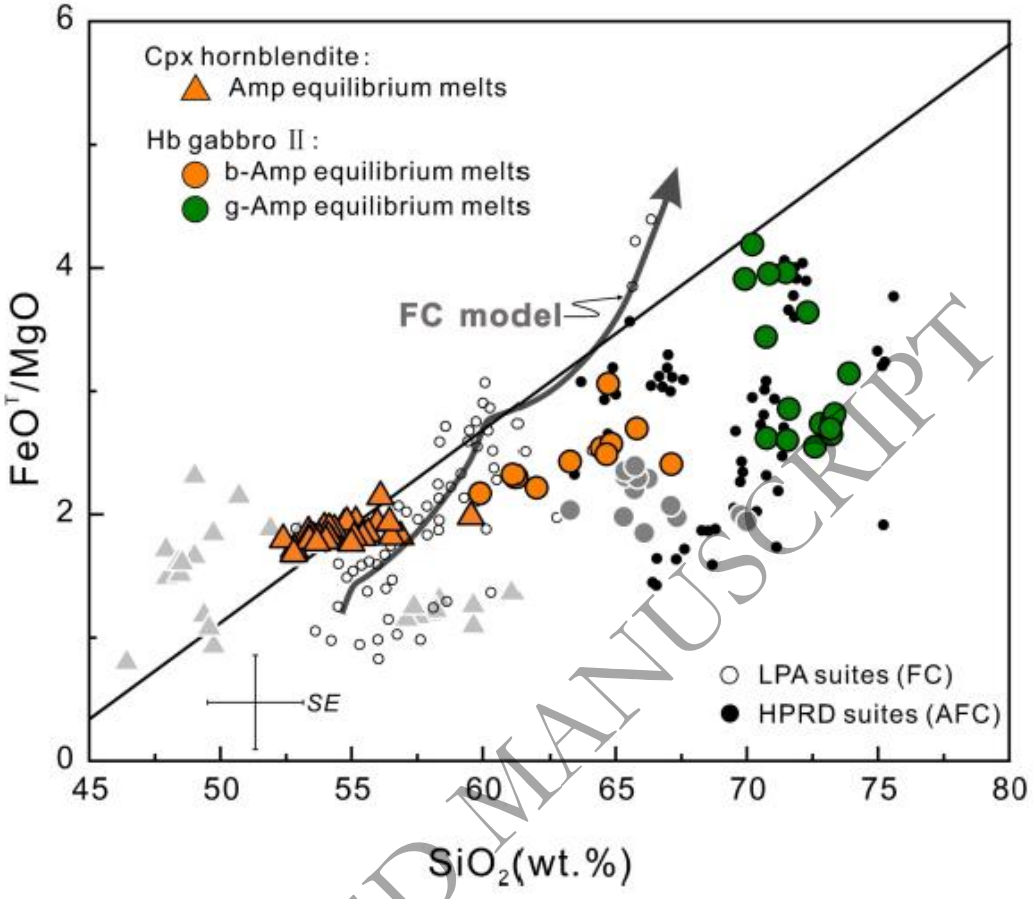

1573

1574

1575 **Fig. 14.**

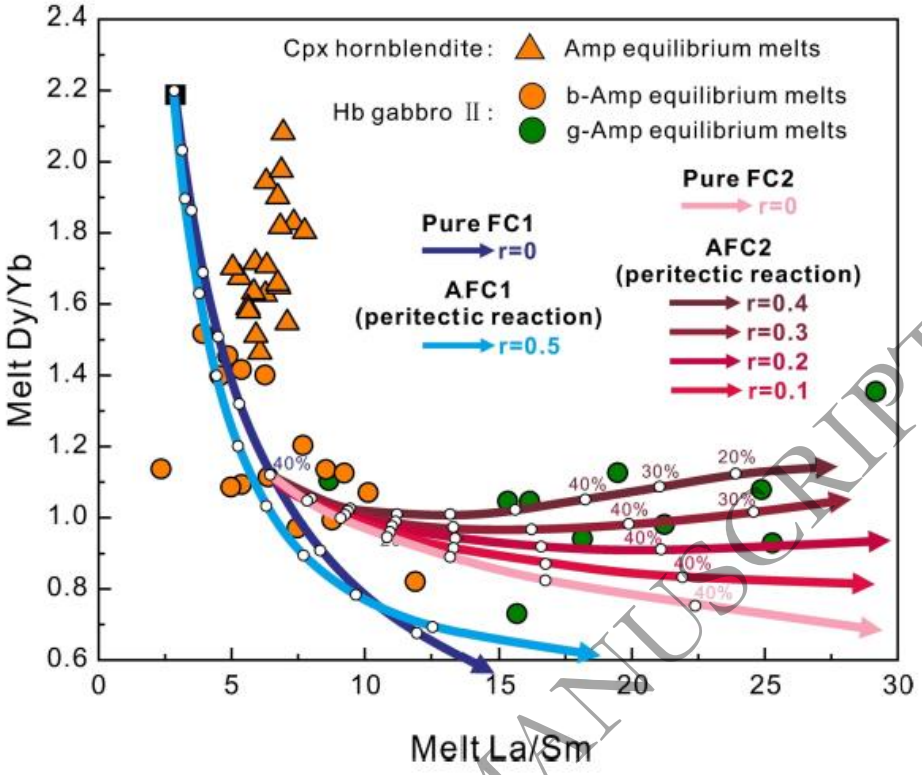

1576

1577

1578 **Fig. 15.**

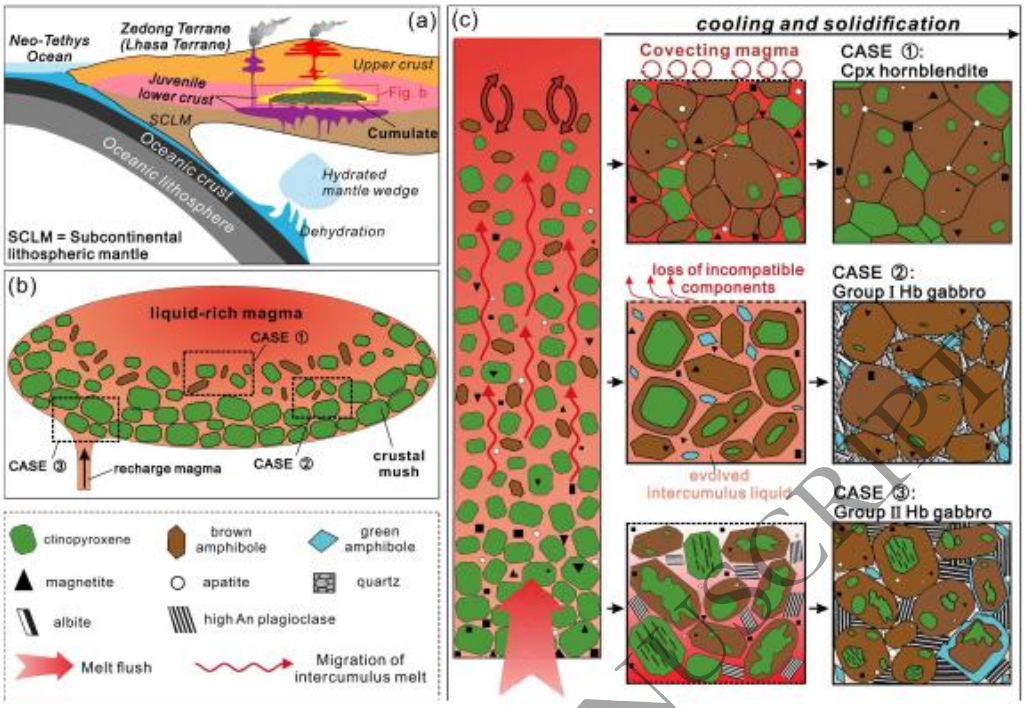

1579

1580

1581

1582

Table 1. Petrographic description of the lithologies of the Zedong Ultramafic–Mafic intrusive rocks.

Lithology	Sample name	Sample location	Longitude(°)	Latitude(°)	texture	Petrographic characteristics	Mineral phases (vol.%)
Cpx hornblendite	09TB01-1	East of Zedong	91.7756	29.2300	adcumulate	Medium- to coarse-grained euhedral Cpx and euhedral to subhedral Amp accumulate in mutual contact, Amp contains some rounded Cpx inclusions and minor Cpx are altered to epidote. Minor subhedral to anhedral Mag and trace anhedral apatite occur within the Amp and Cpx grains or in the interstices between them Medium− to fine−grained Cpx and Medium- to coarse-grained brown Amp including (1) idiomorphic cumulus phase; (2) large Amp oikocryst enclosing rounded Mag and Cpx; (3) minor interstitial anhedral grains (＜5 vol. %)	Cpx (25-30%), Amp (60-65%), Mag (＜10%), trace Ap and Ep
	09TB01-2		91.7756	29.2300			
Hb gabbro I	09TB10-1	East of Zedong	91.7892	29.2269	orthocumulate	Medium- to coarse-grained brown amphibole (＞70%) and fine-grained euhedral to subhedral green amphibole (＜10%). Trace relic Cpx	Amp (70-80%), Pl (15–20%), Qz (5%), Cpx (＜5%)
	09TB11	East of Zedong	91.7889	29.2269			
	09TB15	East of Zedong	91.7886	29.2264			
	09TB16	East of Zedong	91.7886	29.2264			

	09TB 18	East of Zedong	91.78 78	29.2 261		inclusions can also be found in the interior of brown Amp, interstitial green Amp, Qtz and Pl fill in the interstices of brown Hb. Interstitial Pl commonly replaced by Ep and Srt	
	09TB 19	East of Zedong	91.78 75	29.2 261			
	09TB 138-2	West of Zedong	91.75 58	29.2 231			
Hb gabbro II	09TB 09	East of Zedong	91.78 94	29.2 269	orthocumulate	Medium- to coarse-grained, euhedral to subhedral brown Amp contains abundant anhedral relict Cpx inclusions. Enclosed Cpx crystals within brown Amp oikocrysts are typically rounded and embayed. Brown Amps are rimmed by green Amp, and Cpx having disequilibrium dissolution features such as embayed edges and resorption channels. Interstitial plagioclase is mostly altered to clay. Minor matrix minerals are mostly altered to Ep and Srt	Amp (60–65%), Cpx (10–15%), Pl (15–20%), trace Chl and Mag
	09TB 139	West of Zedong	91.75 44	29.2 247			
	09TB 143	West of Zedong	91.68 67	29.2 439			
	09TB 144	West of Zedong	91.68 67	29.2 439			

Cpx, clinopyroxene; Hb, hornblende; Pl, plagioclase; Mag, magnetite; Qtz, quartz; Ap, apatite; Chl, chlorite; Ep, epidote; Srt, sericite.

1583

1584

Table 2. Whole-rock geochemical data of ultramafic-mafic intrusive rocks from the Zedong terrane, southern Tibet

Sample	09TB01-1	09TB01-2	09TB10-1	09TB11	09TB15	09TB16	09TB18	09TB19	09TB138-2	09TB09	09TB139	09TB143	09TB144
Geochemical suite			I	I	I	I	I	I	I	II	II	II	II
wt %													
SiO_2	38.87	39.99	50.1	43.5	49.5	51.4	45.1	46.66	43.7	45.6	45.9	45.4	46.5
TiO_2	1.29	1.64	0.600	0.830	0.680	0.650	0.790	0.870	1.03	0.550	0.650	0.840	1.03
Al_2O_3	14.7	9.30	17.5	16.8	19.3	17.1	17.3	17.0	18.0	9.56	12.9	13.0	15.7
$Fe_2O_3^T$	15.2	16.8	8.60	12.0	9.74	9.86	13.3	12.1	12.8	12.3	10.6	11.0	8.90
MnO	0.150	0.160	0.140	0.140	0.150	0.150	0.170	0.150	0.200	0.210	0.170	0.190	0.140
MgO	8.37	12.0	5.00	6.76	3.98	4.70	6.06	5.73	6.35	13.1	10.8	12.8	10.7
CaO	16.4	16.5	9.89	13.7	7.52	8.32	11.1	9.97	10.7	13.7	10.5	11.3	10.0
Na_2O	0.890	0.730	3.56	1.54	3.32	2.25	1.72	1.77	1.43	1.16	2.11	1.41	1.25
K_2O	0.630	0.530	1.17	0.730	2.19	2.23	1.22	1.75	2.26	0.280	1.66	1.00	2.46
P_2O_5	0.630	0.200	0.170	0.0500	0.320	0.110	0.0700	0.0800	0.360	0.0400	0.480	0.120	0.0600
LOI	2.63	1.79	3.08	3.51	3.05	2.95	2.81	3.58	2.77	3.16	3.79	2.66	2.84
Total	99.6	99.5	99.8	99.7	99.7	99.7	99.6	99.6	99.6	99.6	99.5	99.6	99.6
$Mg^{\#}$	52	58	54	53	45	49	47	49	50	68	67	70	71
μg/g													
Sc	42.6	89.1	22.7	38.7	14.2	23.4	25.3	32.0	34.1	55.6	36.3	49.9	49.8
Ti	7570	9930	4170	4960	3920	4000	4580	5100	3560	4220	6040	5260	6100
V	398	484	207	288	193	250	275	268	261	254	356	313	302

Cr	96.2	156	107	17.9	12.1	26.2	15.8	22.1	63.1	394	399	533	385
Co	56.0	73.1	48.9	46.8	41.4	52.8	63.9	60.6	56.2	71.8	44.1	57.2	47.7
Ni	37.6	63.9	50.9	40.3	10.1	27.1	25.2	22.1	17.9	156	331	245	193
Ga	14.9	14.1	14.9	15.3	16.5	14.8	15.5	15.5	14.4	10.5	18.0	13.9	14.6
Ge	1.46	2.17	1.34	1.49	1.42	1.43	1.44	1.34	1.65	1.71	1.52	1.61	1.57
Rb	6.46	4.07	33.4	17.2	47.5	48.2	22.8	35.5	25.7	2.06	60.0	22.9	68.4
Sr	616	293	455	561	439	375	391	438	576	198	506	447	495
Y	13.7	16.3	15.1	12.6	21.0	14.2	17.7	14.3	17.9	12.9	23.0	17.8	18.3
Zr	23.3	39.6	75.7	30.9	47.1	53.3	41.9	39.1	51.8	39.2	69.3	43.4	41.9
Nb	2.19	2.20	2.17	1.04	1.89	1.47	1.17	2.03	4.61	1.22	3.85	1.72	1.79
Cs	0.610	0.226	1.09	0.830	2.58	2.69	1.23	1.64	0.267	0.397	1.74	0.405	1.21
Ba	226	172	572	330	641	604	453	969	568	942	280	333	884
La	4.14	3.89	10.7	4.13	9.73	7.15	4.57	5.15	12.3	4.08	13.4	8.59	7.78
Ce	11.9	12.3	20.6	9.61	20.4	14.2	10.3	11.0	26.0	9.79	29.0	19.2	17.8
Pr	2.01	2.31	2.53	1.39	2.71	1.79	1.48	1.51	3.32	1.42	3.97	2.55	2.42
Nd	10.6	12.6	10.5	6.99	12.3	7.67	7.48	7.18	13.2	6.53	16.1	11.2	10.4
Sm	2.97	3.61	2.46	2.03	3.14	1.96	2.24	1.98	3.00	1.81	3.85	2.89	2.90
Eu	0.996	1.19	0.899	0.760	1.18	0.768	0.899	0.840	1.06	0.645	1.37	1.03	1.08
Gd	3.04	3.83	2.55	2.27	3.46	2.25	2.76	2.33	3.03	2.07	4.06	3.21	3.41
Tb	0.524	0.631	0.451	0.410	0.631	0.417	0.516	0.429	0.523	0.385	0.685	0.542	0.559
Dy	2.99	3.68	2.80	2.47	3.92	2.60	3.24	2.72	3.07	2.47	3.97	3.20	3.30
Ho	0.570	0.698	0.591	0.503	0.828	0.542	0.684	0.583	0.625	0.516	0.815	0.662	0.677

Er	1.41	1.73	1.70	1.37	2.30	1.56	1.96	1.58	1.79	1.45	2.29	1.71	1.82
Tm	0.182	0.226	0.259	0.193	0.343	0.231	0.273	0.237	0.257	0.215	0.329	0.244	0.252
Yb	1.11	1.37	1.75	1.27	2.22	1.59	1.77	1.54	1.71	1.43	2.16	1.57	1.63
Lu	0.159	0.205	0.287	0.189	0.352	0.256	0.272	0.243	0.267	0.227	0.332	0.245	0.245
Hf	1.14	1.97	2.20	1.06	1.46	1.56	1.28	1.30	1.52	1.26	1.96	1.46	1.48
Ta	0.170	0.190	0.224	0.104	0.144	0.183	0.118	0.230	0.317	0.116	0.243	0.135	0.147
Pb	2.56	0.747	5.74	2.14	4.08	3.29	2.01	3.34	4.05	1.40	5.11	2.27	6.83
Th	0.190	0.115	4.08	1.05	1.89	2.66	1.24	1.57	2.12	1.28	2.76	1.12	0.586
U	0.102	0.0970	1.03	0.370	0.462	0.753	0.426	0.476	0.796	0.334	0.783	0.314	0.156
δEu	1.01	0.97	1.18	1.08	1.09	1.12	1.11	1.19	1.07	1.02	1.06	1.03	1.05
$(La/Yb)_N$	2.69	2.04	4.38	2.34	3.14	3.23	1.85	2.41	5.17	2.05	4.43	3.92	3.42
$(Dy/Yb)_N$	1.80	1.80	1.07	1.30	1.18	1.09	1.23	1.18	1.20	1.16	1.23	1.36	1.36
$^{87}Sr/^{86}Sr$	0.704088	0.704142			0.704934					0.704682		0.704809	
2σ	0.000015	0.000015			0.000011					0.000014		0.000013	
$(^{87}Sr/^{86}Sr)_i$	0.704	0.7041			0.7042					0.7046		0.7045	
$^{143}Nd/^{144}Nd$	0.512928	0.512909			0.512129					0.512886		0.512879	
2σ	0.000009	0.000001			0.000008					0.000009		0.000008	

$\varepsilon_{Nd}(t)$	6.2	5.7 7	5.9 7	5.4 4	5.5 2
T_{DM}(Ga)	77 5	91 0	64 3	86 9	72 3

$Fe_2O_3^T$ = Total iron measured as Fe_2O_3.
LOI = loss on ignition.
$Mg^{\#}$ = 100 × $Mg^{2+}/(Mg^{2+} + Fe^{2+})$

Chondritic uniform reservoir (CHUR) values [$^{143}Nd/^{144}Nd$ = 0.512638, $^{147}Sm/^{144}Sm$ = 0.1967 (Patchett *et al*., 2004)] are used for the calculation. λ_{Rb} = 1.42 X 10^{-11} $year^{-1}$, λ_{Sm} = 6.54 X 10^{-12} $year^{-1}$ (Lugmair & Harti, 1978).

1585